



# A discrete differential geometry-based numerical framework for extensible ribbons

Weicheng Huang<sup>a,c</sup>, Chao Ma<sup>d</sup>, Qiang Chen<sup>a,c</sup>, Longhui Qin<sup>a,b,\*</sup>

<sup>a</sup> School of Mechanical Engineering, Southeast University, Nanjing, 211189, China

<sup>b</sup> State Key Laboratory of Fluid Power and Mechatronic Systems, Zhejiang University, Hangzhou, 310027, China

<sup>c</sup> Jiangsu Engineering Research Center of Aerospace Machinery, Southeast University, Nanjing, 211189, China

<sup>d</sup> School of Electronics, Peking University, Beijing, 100871, China

## ARTICLE INFO

### Keywords:

Elastic ribbon  
Discrete model  
Numerical simulation  
Geometrical nonlinearity  
Bifurcation

## ABSTRACT

As a typical mechanical structure, ribbons are characterized with three distinctly different dimensions, i.e., length  $\gg$  width  $\gg$  thickness, which leads to their exclusive behaviors different from the one-dimensional (1D) case of slender rods and the two-dimensional (2D) case of thin plates. In this paper, we report a discrete differential geometry (DDG)-based numerical method to simulate the geometrically nonlinear deformations of extensible ribbons. With a cross section-dependent regularized parameter introduced, the proposed 1D framework allows both in-plane stretching and out-of-plane bending in the ribbon mid-surface, aimed at bridging the gap between the linear Kirchhoff rod theory and the developable Sadowsky ribbon model. Instead of solving the ordinary differential equations (ODEs) directly with the associated boundary conditions, the mechanical object is discretized into a mass-spring system, and its equilibrium configuration is obtained through a dynamic relaxation method. The numerical framework is applied to seven typical occasions based on either experimental or published datasets in order to verify its performance. Quantitative agreements demonstrate the effectiveness and accuracy of the proposed discrete approach for extensible ribbons, which, as a computationally efficient numerical simulator, could provide a pivotal understanding of a batch of slender structures, and further inspire the simulation-guided design of man-made systems.

## 1. Introduction

Ribbons, or called strips, appear as an intermediate form between 1D rod theory and 2D plate model, since their three dimensions are distinctly different (Dias and Audoly, 2015). Ribbon-like structures are ubiquitous in our daily life, e.g., paper strips, belts, and children's toys (Dias and Santangelo, 2012; Dias et al., 2012; Dias and Audoly, 2014; Shen et al., 2015). Two representative configurations of deformed ribbons can be found in Fig. 1. As a typical mechanical structure, extensible ribbons possess some exclusive properties and the research on their geometrically nonlinear deformations becomes significant since it could motivate a fundamental understanding of biophysical investigations (e.g., DNA helical structures Tanaka and Takahashi (1985), Wadati and Tsuru (1986), Tobias et al. (1994), Starostin (1996), Manning and Maddocks (1999), Hoffman et al. (2003), Coleman and Swigon (2004) and Han et al. (2010) and bacterial flagella (Zhang et al., 2009; Koens and Lauga, 2016), and assist the design and control of engineered systems (for instance, metamaterials (Cattaneo et al., 2008; Wang et al., 2010; Wu et al., 2013) and stretchable

electronics (Nan et al., 2018; Li et al., 2019; Han et al., 2019; Zhao et al., 2019).

From a mechanical perspective, the model of elastic ribbons stays halfway between the 1D elastic rod (with length  $l \gg$  width  $w \sim$  thickness  $b$ ) and 2D elastic plate or shell (with  $l \sim w \gg b$ ), i.e., it looks like an anisotropic rod in the longitudinal direction while behaves similar to a narrow plate in the transverse direction (Dias and Audoly, 2015). It is straightforward to employ Kirchhoff rod equations for the exploration of nonlinear mechanics of a narrow strip, and a variety of existing investigations on Kirchhoff theory can be found, e.g., Kehrbaum and Maddocks (1999), Ameline et al. (2017), Nizette and Goriely (1999), and Antman and Kenney (1981), Antman and Jordan (1975). Moreover, previous analytical, numerical, and experimental investigations demonstrated that the deformed configurations of 1D rod-like structures in both isotropic cross section (Van der Heijden and Thompson, 2000; Van der Heijden et al., 2003; Goyal et al., 2005) and anisotropic cross section (Buzano, 1986; Van der Heijden and Thompson, 1998; Béda et al., 1992; Goriely et al., 2001; Yu and Hanna, 2019;

\* Corresponding author.

E-mail address: [lhqin@seu.edu.cn](mailto:lhqin@seu.edu.cn) (L. Qin).

<https://doi.org/10.1016/j.ijsolstr.2022.111619>

Received 20 August 2021; Received in revised form 7 April 2022; Accepted 11 April 2022

Available online 18 April 2022

0020-7683/© 2022 Elsevier Ltd. All rights reserved.

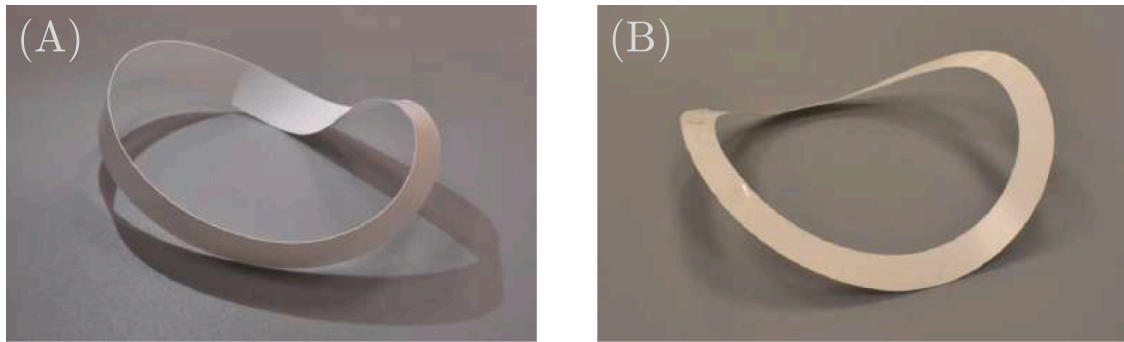


Fig. 1. Two representative deformed configurations in elastic ribbons (Photos from our experiment). (A): Möbius strip. (B): Buckling instability of an undercurve annular ribbon.

Xu et al., 2019; Huang et al., 2021a) could be described accurately by a group of ODEs formulated from the Kirchhoff model. However, the classical Kirchhoff rod framework is only justified from three-dimensional (3D) elasticity assuming that the structural width and thickness are in the same order of magnitude,  $w/b \sim O(1)$ . Sadowsky ribbon framework (Sadowsky, 1930), on the other hand, assumes that the ribbon mid-surface is developable and fully inextensible, as a result of which it is valid for structures with a large enough width-to-thickness ratio,  $w/b \rightarrow \infty$ . Whereas, its prediction on the structural inflection point is discontinuous and singular (Starostin and van der Heijden, 2015; Yu and Hanna, 2019; Huang et al., 2020b), and may fail for the predictions of real objects with non-zero thickness. Similar problems were found for Wunderlich energy functional (Wunderlich, 1962; Starostin and Van Der Heijden, 2007; Starostin and van der Heijden, 2008; Moore and Healey, 2015), which was an extension of Sadowsky model. The gap between the Kirchhoff rod model and Sadowsky ribbon model could be fulfilled by either 2D plate simulation (Huang et al., 2020b) or 1D reduced order model (Sano and Wada, 2019; Audoly and Neukirch, 2021). The relation of different theories is illustrated in Fig. 2. Quite recently, Neukirch and Audoly (2021) demonstrated that the deformed configuration of a thin elastic ribbon could be accurately described by its centerline curvatures. The 1D centerline-based energy functional originally proposed by Sano and Wada (2019) and Audoly and Neukirch (2021) properly characterizes the deformation of extensible ribbons, i.e., the mid-surface of a ribbon is stretchable rather than developable.

The 1D equilibrium problems in structural mechanics are usually derived by solving the ODEs with associated boundary conditions through either an analytical or a numerical approach, e.g., AUTO — a continuous numerical package (Doedel, 2007). However, it became a painstaking trial to solve the BVP directly from the results of functional variation, especially when geometric nonlinearity is involved. Finite Element Method (FEM) was then developed to systemically investigate the complex mechanical responses in both solids and structures (Wood and Zienkiewicz, 1977; Bonet and Wood, 1997; Zienkiewicz and Taylor, 2005; Hughes, 2012; De Borst et al., 2012; Liu et al., 2019). Some other numerical frameworks, such as Geometrically Exact Beam Formulation (GEBF) (Simo, 1985; Simo and Vu-Quoc, 1986), Absolute Nodal Coordinate Formulation (ANCF) (Shabana, 1996; Tang et al., 2021; Sun et al., 2019; Luo et al., 2017), Isogeometric Collocation (Kiendl et al., 2015; Auricchio et al., 2016), and Mixed Isogeometric Finite Element Method (Greco and Cuomo, 2016), were also used to address the mechanics of thin elastic structures that underwent finite deflection and rotation. In this decade, another type of numerical framework – DDG-based formulation – is becoming increasingly popular in both computer geometry and computer graphics communities, due to its robustness, accuracy, and efficiency in simulating the geometrically nonlinear deformations of thin elastic structures, e.g. hairs and clothes. The computationally efficient DDG method first discretizes a continuous curve (or surface) into multiple nodes and

edges, maintaining its key geometric information to capture the non-linear deformations, e.g., bending curvatures. Then, the target object is modeled as a mass-spring system, such that its dynamic performance can be easily achieved by integrating the discrete equations of motion (Huang and Jawed, 2019). Notice that the shape function used in FEM is usually a high order polynomial and is differentiable, such that the elastic potentials can be derived directly by taking the derivative of shape function; DDG method, on the other side, is  $C_1$  continuous (e.g., position only), and, therefore, the energy can only be given on the basis of nodal positions (and twist angles in 3D case). Nevertheless, DDG can be treated as a special FEM with a piece-wise linear (or even constant) shape function. Previous DDG-based formulations have shown powerful performances in simulating thin elastic bodies, e.g. rods (Bergou et al., 2008, 2010; Audoly and Pomeau, 2010; Audoly et al., 2013; Jawed et al., 2014; Huang et al., 2020a), developable ribbons (Shen et al., 2015; Charrondière et al., 2020; Kumar et al., 2021), plates/shells (Baraff and Witkin, 1998; Grinspun et al., 2003; Bridson et al., 2005; Huang et al., 2020b), and gridshells/Cosserat nets (Baek et al., 2018; Baek and Reis, 2019; Panetta et al., 2019; Huang et al., 2021b). Romero et al. quantitatively verified these computer graphics simulators through extensive experiments which validated the success of DDG-based frameworks in engineering problems (Romero et al., 2021).

In this paper, the well-known Discrete Elastic Rods (DER) algorithm (Bergou et al., 2008, 2010) is adapted to simulate the geometrically nonlinear deformation of extensible ribbons. The 1D structures (e.g., rods and ribbons) can be geometrically described with a space curve called centerline and an associated orthonormal material frame, based on which the strain measurements (bending, twisting, and stretching) formulated in DER framework can be translated to capture the deformed configurations of all 1D objects directly (Audoly and Pomeau, 2010). The constitutive relations for extensible ribbon framework, on the other side, are different from the naive Kirchhoff rod theory, i.e., the total potentials in linear rod model are related to the quadratic forms of strains, while the elastic energies for extensible ribbons is derived from the 2D plate theory (Audoly and Neukirch, 2021). A set of equations of motion established from the statement of force balance are numerically updated by a first order implicit Euler method (Huang and Jawed, 2019). The equilibrium configurations are eventually obtained with damping forces added into the system, known as dynamic relaxation method. As the inertial effect is considered, the established framework is able to automatically capture the bifurcations between the stable and unstable phases by introducing some small disturbances (Huang et al., 2020b). The gradient associated with internal elastic force and the Hessian associated with Jacobian matrix of elastic potentials are analytically derived, resulting in a fully implicit algorithm, and the Hessian of it is a banded matrix, which can be solved in linear complexity. By way of demonstrations, we consider seven occasions including: (i) cantilever beams under gravity; (ii) circular ribbons under gravity; (iii) overcurve and undercurve in annular ribbons; (iv) lateral-torsional buckling of beams; (v) Möbius

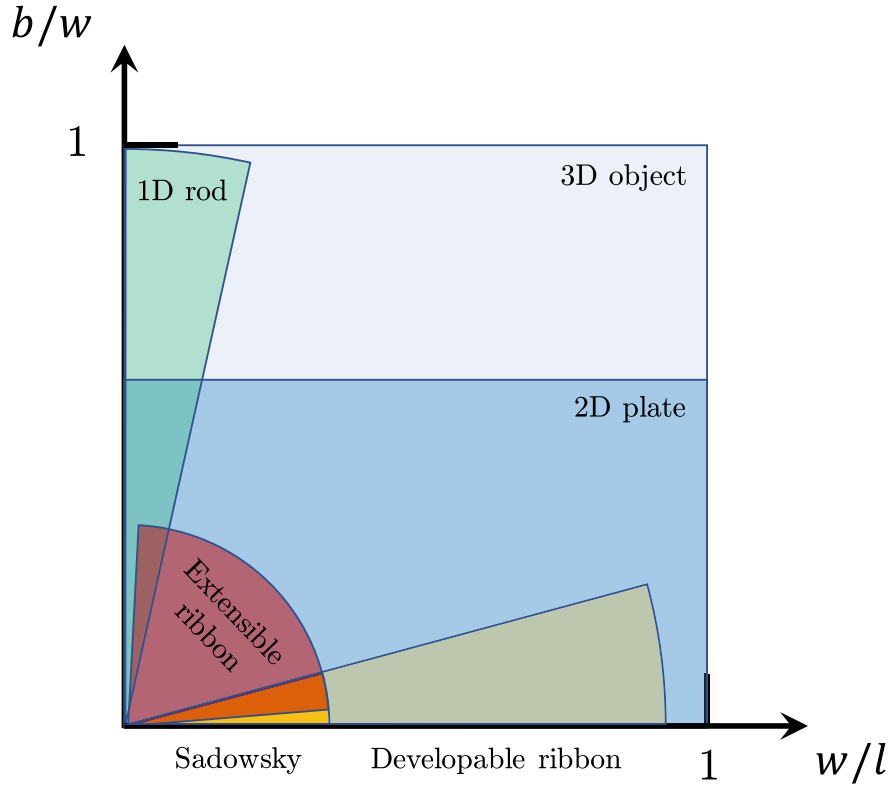


Fig. 2. Geometric map of different theories for an elastic body with a rectangular cross-section (Audoly and Neukirch, 2021). Here, the structural length, width, and thickness are  $l$ ,  $w$ , and  $b$ , separately. This paper focuses on the simulation in extensible ribbons (red area).

strips; (vi) shear induced bifurcation of pre-buckled ribbons; and (vii) twist-induced snapping in bent ribbons, to comprehensively show the performance of our newly introduced extensible ribbon simulator. Discrete simulators based on linear Kirchhoff rod theory and developable Sadowsky ribbon theory are further included, for a general comparison among all different 1D models. Moreover, quantitative agreements have been found between our numerical predictions and experimental data (or published data).

The other parts of this paper are organized as follows. Section 2 depicts the DDG-based discretization and the simulating procedure for extensible ribbons. Demonstrations for the well-established framework are systemically presented and discussed in Section 3, after which conclusive remarks and future research directions are summarized in Section 4. The analytical formulation for extensible ribbons is reviewed in Appendix A.

## 2. Discrete model

In this section, a discrete framework is implemented to explore the mechanical response of extensible ribbons, which is based on the continuous model formulated in Appendix A. The structure considered herein is of length  $l$ , width  $w$ , thickness  $b$ , and the material is isotropic, linearly elastic. The Young's modulus is represented by  $E$  and Poisson's ratio by  $\nu$ . Specifically, the elastic ribbon is treated as a mass-spring-damper system and both space and time discretizations are employed. Then, the equilibrium configuration is derived through a dynamic relaxation method. The discretized procedure is similar to the well-known DER algorithm (Bergou et al., 2008, 2010).

### 2.1. Elastic energies

A continuous strip is discretized into  $N$  nodes,  $\mathbf{x}_0, \dots, \mathbf{x}_{N-1}$ , and  $N-1$  edge vectors,  $\mathbf{e}^0, \dots, \mathbf{e}^{N-2}$ , resulting in  $\mathbf{e}^i = \mathbf{x}_{i+1} - \mathbf{x}_i$  and  $i = 0, \dots, N-2$ .

Hereafter, subscripts are adopted for the quantities associated with nodes, e.g.,  $\mathbf{x}_i$ ; and superscripts are for the quantities associated with edges, e.g.,  $\mathbf{e}^i$ . Each edge,  $\mathbf{e}^i$ , has an orthonormal adapted reference frame  $\{\mathbf{d}_1^i, \mathbf{d}_2^i, \mathbf{d}_3^i\}$  and a material frame  $\{\mathbf{m}_1^i, \mathbf{m}_2^i, \mathbf{m}_3^i\}$ , both of which share the tangential direction,  $\mathbf{d}_3^i \equiv \mathbf{m}_3^i = \mathbf{e}^i/|\mathbf{e}^i|$ . Difference of the two frames is  $\theta^i$  as shown in Fig. 3. Node positions as well as twist angles constitute the  $4N-1$  sized degrees of freedom (DOF) vector,  $\mathbf{q} = [\mathbf{x}_0, \theta^0, \mathbf{x}_1, \dots, \mathbf{x}_{N-2}, \theta^{N-2}, \mathbf{x}_{N-1}]$ .

The strains of a deformed strip comprise three parts: stretching, bending, and twisting. At first, the discrete stretching strain associated with the  $i$ th edge,  $\mathbf{e}^i$ , is

$$\epsilon^i = \frac{|\mathbf{e}^i|}{|\bar{\mathbf{e}}^i|} - 1, \quad (1)$$

where the quantity with a bar on top indicates its undeformed configuration. Next, the discrete bending strain is captured by the curvature binormal that measures the misalignment between two consecutive edges at  $\mathbf{x}_i$ ,

$$(\kappa \mathbf{b})_i = \frac{2\mathbf{e}^{i-1} \times \mathbf{e}^i}{|\mathbf{e}^{i-1}| |\mathbf{e}^i| + \mathbf{e}^{i-1} \cdot \mathbf{e}^i}, \quad (2)$$

and its norm is  $|\kappa \mathbf{b}| = 2 \tan(\phi_i/2)$ , referring to Fig. 3. The material curvatures are given by the inner products of the curvature binormal and the material frame,

$$\kappa_{1,i} = \frac{1}{2} (\mathbf{m}_2^{i-1} + \mathbf{m}_2^i) \cdot (\kappa \mathbf{b})_i, \quad (3a)$$

$$\kappa_{2,i} = -\frac{1}{2} (\mathbf{m}_1^{i-1} + \mathbf{m}_1^i) \cdot (\kappa \mathbf{b})_i. \quad (3b)$$

Finally, the discrete twisting strain at the  $i$ th node is measured using the discrete twist,

$$\kappa_{3,i} = \theta^i - \theta^{i-1} + m_i^{\text{ref}}, \quad (4)$$

where  $m_i^{\text{ref}}$  is the reference twist associated with the reference frame and can be computed from a parallel transport (Bergou et al., 2008,

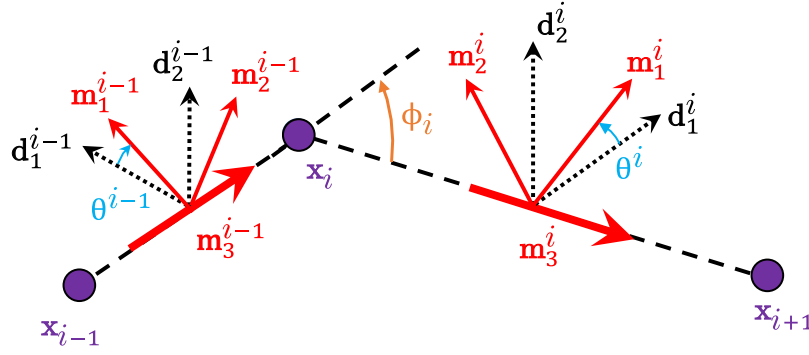


Fig. 3. Notations used in our discrete model.

2010; Jawed et al., 2018). As a friendly reminder, the curvatures formulated above,  $\kappa_{\alpha,i}$  with  $\alpha \in \{1, 2, 3\}$ , are non-dimensional, i.e., the physical curvatures should be  $\kappa_{\alpha,i}/\Delta l_i$ , where  $\Delta l_i = (|\bar{\mathbf{e}}^i| + |\bar{\mathbf{e}}^{i-1}|)/2$  is the Voronoi length associated with the  $i$ th node,

Based on the formulations of discrete strains and the energy functional provided in Appendix A (Eqs. (A.3) and (A.7)), the discrete formats of the elastic energies for an extensible ribbon are given as follows,

$$E_{\text{stretch}} = \sum_{i=0}^{N-2} E_{\text{stretch}}^i = \frac{1}{2} \sum_{i=0}^{N-2} EA (\epsilon^i)^2 |\bar{\mathbf{e}}^i|,$$

$$E_{\text{ribbon}} = \sum_{i=1}^{N-2} E_{\text{ribbon},i}$$

$$= \frac{1}{2} \sum_{i=1}^{N-2} \frac{1}{\Delta l_i} \left[ EI_1 (\kappa_{1,i})^2 + EI_2 (\kappa_{2,i})^2 + GJ (\kappa_{3,i})^2 + \frac{EI_2}{1-\nu^2} \frac{(\nu \kappa_{2,i}^2 + \kappa_{3,i}^2)^2}{\frac{60}{1-\nu^2} \frac{b^2}{w^3} + \kappa_{2,i}^2} \right], \quad (5)$$

where  $EA = Ewb$  is the stretching stiffness,  $EI_1 = E \frac{1}{12} bw^3$  is the bending stiffness around the surface normal,  $EI_2 = E \frac{1}{12} wb^3$  is the bending stiffness around the edge vector, and  $GJ = \frac{E}{2(1+\nu)} \frac{1}{3} wb^3$  is the twisting stiffness around the centerline tangent ( $J = \frac{1}{3} wb^3$  for a rectangular cross section with  $w \gg b$ ). Here, both  $EA$  and  $EI_1$  are much larger than  $EI_2$  and  $GJ$ , acting as penalty terms.

## 2.2. Gradient and Hessian matrix of elastic energies

The gradient vector,  $\partial E_{\text{total}}/\partial \mathbf{q}$ , as well as the Hessian matrix,  $\partial^2 E_{\text{total}}/\partial \mathbf{q}^2$ , of elastic energies in Eq. (5) is formulated next, where  $E_{\text{total}} = E_{\text{stretch}} + E_{\text{ribbon}}$  is the sum of elastic potentials. The energy gradient at the  $j$ th DOF ( $0 \leq j \leq 4N - 1$ ) is given utilizing the chain rule,

$$\frac{\partial E_{\text{total}}}{\partial q_j} = \sum_{i=0}^{N-2} \frac{\partial E_{\text{stretch}}^i}{\partial \epsilon^i} \frac{\partial \epsilon^i}{\partial q_j} + \sum_{i=1}^{N-2} \frac{\partial E_{\text{ribbon},i}}{\partial \kappa_{\alpha,i}} \frac{\partial \kappa_{\alpha,i}}{\partial q_j}, \quad (6)$$

where  $\kappa_{\alpha,i}$  is the discrete curvatures at the  $i$ th node, e.g.,  $\kappa_{1,i}$ ,  $\kappa_{2,i}$ , and  $\kappa_{3,i}$ . The Einstein summation convention for  $\alpha$  index is followed,

$$\frac{\partial E_{\text{ribbon},i}}{\partial \kappa_{\alpha,i}} \frac{\partial \kappa_{\alpha,i}}{\partial q_j} = \frac{\partial E_{\text{ribbon},i}}{\partial \kappa_{1,i}} \frac{\partial \kappa_{1,i}}{\partial q_j} + \frac{\partial E_{\text{ribbon},i}}{\partial \kappa_{2,i}} \frac{\partial \kappa_{2,i}}{\partial q_j} + \frac{\partial E_{\text{ribbon},i}}{\partial \kappa_{3,i}} \frac{\partial \kappa_{3,i}}{\partial q_j}. \quad (7)$$

The material-related terms,  $\frac{\partial E_{\text{stretch}}^i}{\partial \epsilon^i}$  and  $\frac{\partial E_{\text{ribbon},i}}{\partial \kappa_{\alpha,i}}$ , can be analytically evaluated from Eq. (5) by symbolic calculator (e.g., Maple or Mathematica). For instance,  $\frac{\partial E_{\text{stretch}}^i}{\partial \epsilon^i} = EA \epsilon^i |\bar{\mathbf{e}}^i|$ . The geometry-related terms,  $\frac{\partial \epsilon^i}{\partial q_j}$  and  $\frac{\partial \kappa_{\alpha,i}}{\partial q_j}$ , on the other hand, are formulated based on the DDG theory (Bergou et al., 2008, 2010), which can be found in Appendix B. It should be noted that the size of non-zero components of  $\partial E_{\text{stretch}}^i/\partial \mathbf{q}$  and  $\partial E_{\text{ribbon},i}/\partial \mathbf{q}$  are 7 and 11, separately.

Moving forward, the  $(j, k)$ -th entry in Hessian matrix can be computed by utilizing the chain rule,

$$\frac{\partial^2 E_{\text{total}}}{\partial q_j \partial q_k} = \sum_{i=0}^{N-2} \left[ \frac{\partial E_{\text{stretch}}^i}{\partial \epsilon^i} \frac{\partial^2 \epsilon^i}{\partial q_j \partial q_k} + \frac{\partial^2 E_{\text{stretch}}^i}{\partial \epsilon^i \partial \epsilon^i} \frac{\partial \epsilon^i}{\partial q_j} \frac{\partial \epsilon^i}{\partial q_k} \right] + \sum_{i=1}^{N-2} \left[ \frac{\partial E_{\text{ribbon},i}}{\partial \kappa_{\alpha,i}} \frac{\partial^2 \kappa_{\alpha,i}}{\partial q_j \partial q_k} + \frac{\partial^2 E_{\text{ribbon},i}}{\partial \kappa_{\alpha,i} \partial \kappa_{\beta,i}} \frac{\partial \kappa_{\alpha,i}}{\partial q_j} \frac{\partial \kappa_{\beta,i}}{\partial q_k} \right], \quad (8)$$

where  $\alpha, \beta \in \{1, 2, 3\}$  and it follows the Einstein summation convention. Similarly, the second order material-related terms,  $\frac{\partial^2 E_{\text{stretch}}^i}{\partial \epsilon^i \partial \epsilon^i}$  and  $\frac{\partial^2 E_{\text{ribbon},i}}{\partial \kappa_{\alpha,i} \partial \kappa_{\beta,i}}$  can be given analytically from Eq. (5), e.g.,  $\frac{\partial^2 E_{\text{stretch}}^i}{\partial \epsilon^i \partial \epsilon^i} = EA |\bar{\mathbf{e}}^i|$ ; the second order geometry-related terms are introduced in Appendix C based on DDG (Bergou et al., 2008, 2010). Again, the non-zero components of each  $i$ th elastic stretching energy and elastic ribbon energy in Hessian matrix are of  $7 \times 7$  and  $11 \times 11$ , respectively. The shape of the Hessian matrix of a ribbon system is shown in Fig. 4.

Overall, the gradient vector as well as the Hessian matrix of elastic energies with respect to DOF are analytically formulated, which are essential in solving the dynamic system of extensible ribbons. Moreover, the geometry-related terms are identical for all 1D theories, e.g., Kirchhoff rod theory in Eq. (A.8), extensible ribbon model in Eq. (A.7), and Sadowsky ribbon framework in Eq. (A.9). The only difference is the material-related parameter, which facilitates the numerical implementation to be more convenient for all 1D frameworks.

It is worth mentioning again that the computational procedure of gradient and Hessian is divided into two terms: the geometry-related terms and material-related terms; the geometry-related terms are already formulated in Bergou et al. (2008, 2010) based on DDG theory; however, previous analysis on 1D bodies only considered linear constitutive relation (e.g., Kirchhoff model), we here extend the linear numerical framework to the nonlinear regime, e.g., extensible ribbon model and Sadowsky ribbon model, and treat all 1D models as a whole, with same description for kinematics (curvatures) and different descriptions for constitutive relations. The novelty here is to compute difference material-related parameters (e.g.,  $\{\frac{\partial E_{\text{stretch}}^i}{\partial \epsilon^i}, \frac{\partial^2 E_{\text{stretch}}^i}{\partial \epsilon^i \partial \epsilon^i}, \frac{\partial E_{\text{ribbon},i}}{\partial \kappa_{\alpha,i}}, \frac{\partial^2 E_{\text{ribbon},i}}{\partial \kappa_{\alpha,i} \partial \kappa_{\beta,i}}\}$ ) for different 1D theories.

## 2.3. Equations of motion

In this section, we discuss the equations of motion for extensible ribbon system. At the  $k$ th time step,  $t_k$ , with the DOF vector,  $\mathbf{q}_k$ , and its velocity,  $\dot{\mathbf{q}}_k$  at hand, the equations of motion and DOF vector can be updated from  $t = t_k$  to  $t = t_{k+1}$ ,

$$\mathbf{E} \equiv \mathbf{M} \Delta \mathbf{q}_{k+1} - h \mathbf{M} \dot{\mathbf{q}}_k - h^2 (\mathbf{F}_{k+1}^{\text{int}} + \mathbf{F}_{k+1}^{\text{ext}}) = \mathbf{0} \quad (9a)$$

$$\mathbf{q}_{k+1} = \mathbf{q}_k + \Delta \mathbf{q}_{k+1} \quad (9b)$$

$$\dot{\mathbf{q}}_{k+1} = \frac{1}{h} \Delta \mathbf{q}_{k+1}, \quad (9c)$$

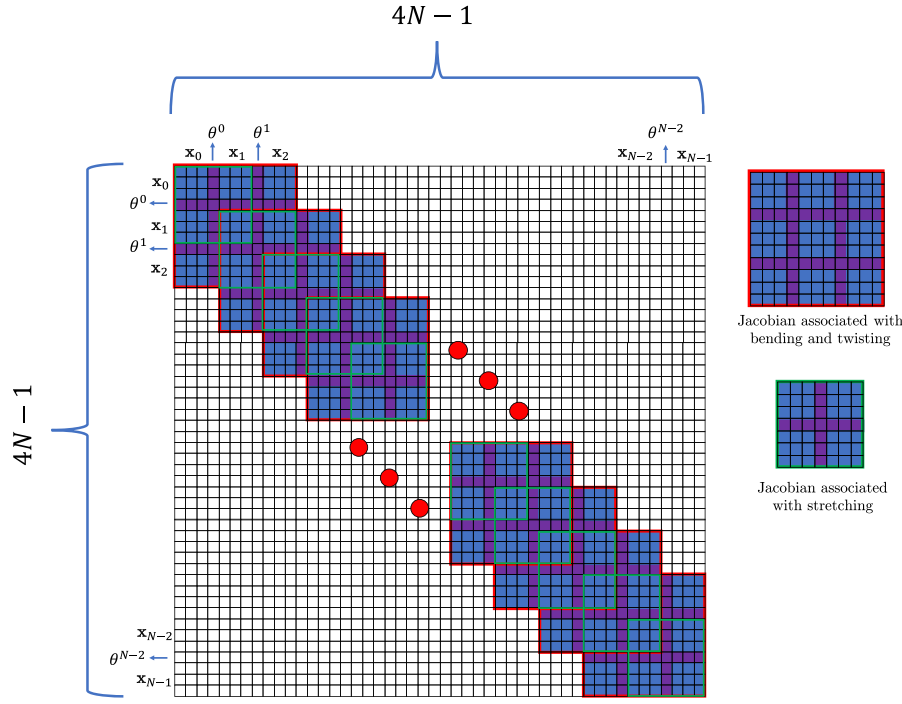


Fig. 4. Shape of Hessian matrix.

where  $\mathbf{E}$  represents the  $4N - 1$  sized equations of motion,  $\mathbf{M}$  is the diagonal mass matrix comprised of lumped masses,  $\mathbf{F}^{\text{int}} = -\partial E_{\text{total}}/\partial \mathbf{q}$  is the internal elastic force in Eq. (6),  $\mathbf{F}^{\text{ext}}$  is the external force vector (e.g., gravity and damping force),  $h$  is the time step size, and the subscript  $k + 1$  (and  $k$ ) denotes the evaluation of the quantity at time  $t_{k+1}$  (and  $t_k$ ).

The Newton-Raphson method is applied to solve this set of nonlinear equations of motion. At the time step  $t_{k+1}$ , a new solution is first guessed on the basis of the previous state, i.e.,

$$\mathbf{q}_{k+1}^{(1)} = \mathbf{q}_k + h\dot{\mathbf{q}}_k. \quad (10)$$

Then, it is optimized utilizing the gradient decent principle, such that the new solution at the  $(n + 1)$ th step is

$$\mathbf{q}_{k+1}^{(n+1)} = \mathbf{q}_{k+1}^{(n)} - \mathbb{J}^{(n)} \backslash \mathbf{E}^{(n)}, \quad (11)$$

where  $\mathbb{J}$  is the Jacobian matrix associated with Eq. (9a),

$$\mathbb{J} \equiv \frac{\partial \mathbf{E}}{\partial \mathbf{q}} = \frac{1}{h^2} \mathbf{M} + \frac{\partial^2 E_{\text{total}}}{\partial \mathbf{q} \partial \mathbf{q}} - \frac{\partial \mathbf{F}^{\text{ext}}}{\partial \mathbf{q}}. \quad (12)$$

The Hessian matrix associated with the total energy is derived in Eq. (8). Referring to Fig. 4, the Jacobian  $\mathbb{J}$  is a banded matrix, which can be solved in linear complexity. This computational efficiency has motivated various applications in the animation industry (e.g., hair simulation for movies) as well as its adoption in mechanical engineering (Jawed et al., 2014). Although this type of numerical framework is established for dynamic simulation, it is still valid for the equilibrium configuration under arbitrary loading and boundary conditions when the damping force is introduced into system.

### 3. Results

In this section, several cases predicted by our simulator are compared with either experimental observations or existing data, in order to verify the effect of our discrete numerical framework for the simulation of extensible ribbons. Meanwhile, the numerical solutions from both linear Kirchhoff model and developable Sadowsky model are established to make a general comparison. The complexity is increased gradually to realize the nonlinear mechanical responses in narrow

strips. The geometrically nonlinear deflection is explored firstly for a clamped-free beam. Then a ribbon with non-zero curvatures in its stress-free configuration is investigated. Finally, the bending-twisting coupling is discussed in details with multiple examples presented.  $N = 100$  vertices are adopted for all demonstrations after a convergent study, and the time step size is  $h = 1$  ms. The numerical tolerance is  $10^{-8}$  and usually 2 or 3 iterations are required during the Newton-Raphson optimization. The computational time of each iteration is approximate 0.18 ms. The simulations are performed on a single thread of Intel Core i7 - 6600U Processor @3.4GHz.

#### 3.1. Cantilever beam under gravity

As shown in Fig. 5(A), a cantilever beam is hung under its own weight. The physical parameters are configured as: length  $l = 200$  mm, width  $w \in \{30, 70, 150\}$  mm, thickness  $b = 0.1$  mm, Young's modulus  $E = 1$  GPa, Poisson's ratio  $\nu = 0.4$ , and gravity  $g = 9.81 \text{ m/s}^2$ . The structural density  $\rho$  is changed to produce different external loadings. The first two nodes,  $\{\mathbf{x}_0, \mathbf{x}_1\}$ , and the first twisting angle,  $\theta^0$ , are fixed to achieve the clamped-free boundary condition in a cantilever beam system. It has also been studied in Shield (1992), Audoly and Neukirch (2021) and Romero et al. (2021). It should be noted that the bending stiffness in Kirchhoff rod theory is  $\frac{Ewb^3}{12}$ , which is different from the Sadowsky framework,  $\frac{Ewb^3}{12(1-\nu^2)}$ , referring to Eqs. (A.8) and (A.9).

Fig. 5(B) shows the displacement of the normalized beam tip,  $\delta/l$ , as a function of the normalized weight,  $\gamma = \frac{\rho w b g l^3}{E w b^3 / 12}$ , comparing the extensible ribbon model of different normalized curvatures,  $1/\kappa^* l \in \{1.43, 7.79, 35.72\}$ , the Kirchhoff rod model, and Sadowsky model. The bending curvature is  $\sim 1/l$ , and  $1/\kappa^* l$  is used to represent the normalized curvature  $|\kappa_2|/\kappa^*$  in 1D slender structures. As for a small value of  $\gamma$ , the structure stays within the geometrically linear regime, and the prediction from Kirchhoff beam model matches well with the analytical solution,  $\delta/l = \frac{1}{8} \frac{\rho w b g l^3}{E w b^3 / 12}$ ; the deflection from Sadowsky framework is slightly smaller than that from the planar beam theory by a relative amount  $\frac{1}{1-\nu^2}$ . The gap between the Kirchhoff model and Sadowsky model can be fulfilled by the presented nonlinear extensible ribbon model as its predicted bending stiffness varies from  $\frac{Ewb^3}{12}$  (In case of



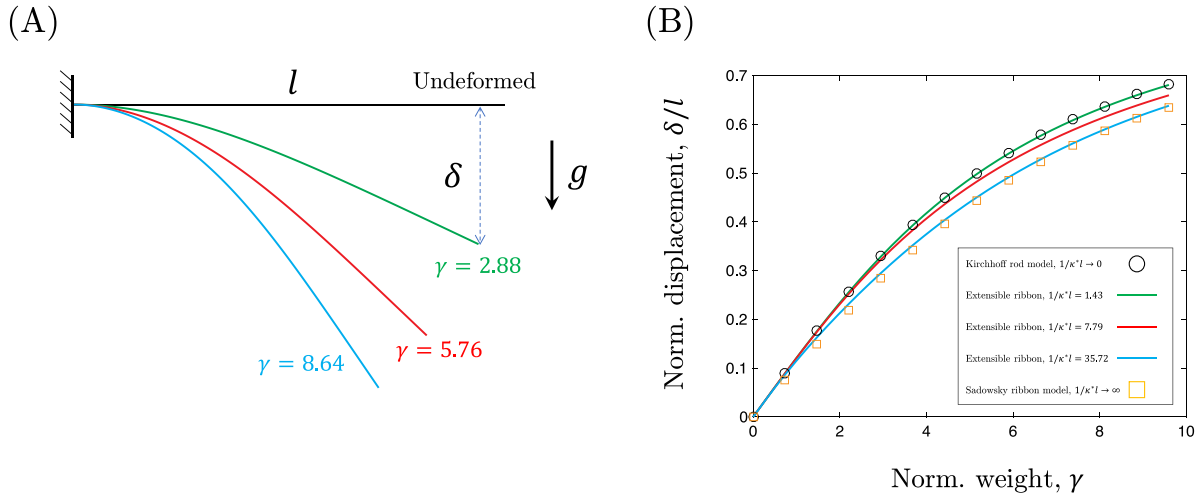


Fig. 5. (A): Deformed patterns of cantilever beams with different normalized weight,  $\gamma \in \{2.88, 5.76, 8.64\}$ . (B): Relations between the normalized displacement,  $\delta/l$ , and the normalized weight,  $\gamma$ , from (i) Kirchhoff rod model; (ii) extensible ribbon framework; and (iii) Sadowsky ribbon theory.

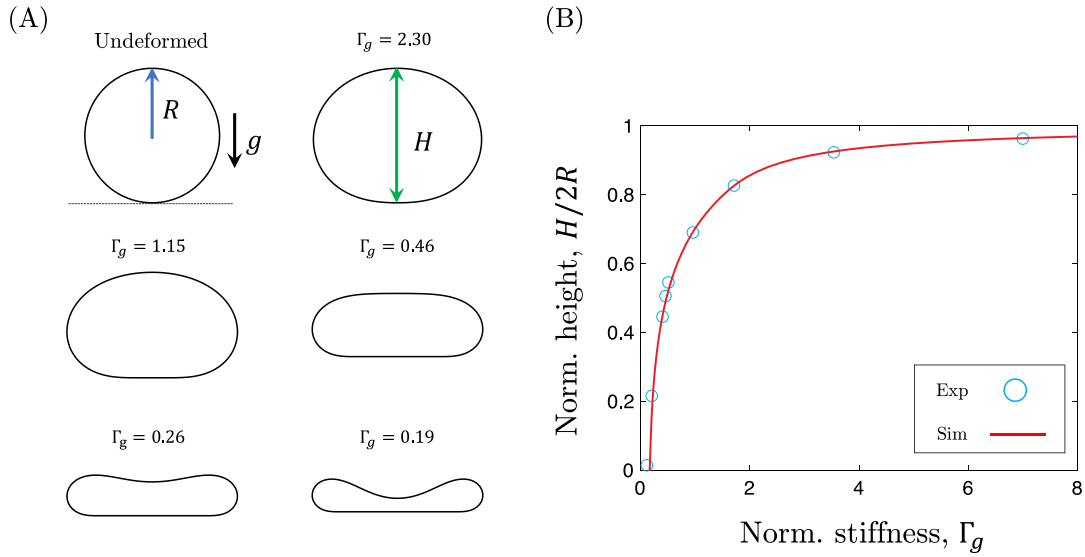


Fig. 6. (A): Deformed configurations of circular ribbons under gravity with different normalized stiffness,  $\Gamma_g \in \{\infty, 2.30, 1.15, 0.46, 0.26, 0.19\}$ . The undeformed shape is when  $\Gamma_g = \infty$ . (B): Relations between the normalized height,  $H/2R$ , and the normalized stiffness,  $\Gamma_g$ , from both numerical approach and tabletop experiments. The experimental data is from Raux et al. (2010).

small strains,  $|\kappa_2|/\kappa^* \sim 0$ , Kirchhoff model) to  $\frac{Ewb^3}{12(1-\nu^2)}$  (In case of large strains,  $|\kappa_2|/\kappa^* \sim \infty$ , Sadowsky model). These results are identical to the Shield's model (Shield, 1992; Audoly and Neukirch, 2021; Romero et al., 2021).

### 3.2. Circular ribbon under gravity

Fig. 6(A) gives the deformation process of a circular ribbon due to its own weight, which is also a planar case but the out-of-plane structural curvature is non-zero in the stress-free configuration,  $\bar{\kappa}_2(S) \neq 0$ . Therefore, the second term in Eq. (5) needs to be slightly modified,  $\sum_{i=1}^{N-2} \frac{1}{2} EI_2 (\kappa_{2,i} - \bar{\kappa}_{2,i})^2$ . Also, the total degrees of freedom in this demonstration are  $4N$  instead of  $4N - 1$ , and the Jacobian matrix is no longer a banded matrix. The elastic stretch energy associated with  $\{\mathbf{x}_0, \mathbf{x}_{N-1}\}$  and the elastic bending and twisting energies associated with  $\{\mathbf{x}_1, \mathbf{x}_0, \mathbf{x}_{N-1}, \mathbf{x}_{N-2}\}$  should be included in the numerical framework. The unilateral contact between the elastic ribbon and the rigid surface is captured by a modified mass method (Huang et al., 2020a, 2021b).

The physical parameters in this numerical test are: ribbon arclength  $l \equiv 2\pi R = 25$  mm, width  $w = 18$  mm, thickness  $b = 1.6$  mm, material density  $\rho = 1000$  kg/m<sup>3</sup>, Poisson's ratio  $\nu = 0.5$ , which are close to the experimental investigations in Raux et al. (2010). The normalized bending curvature here is approximate  $1/\kappa^*l = 3.98$ ; and, according to our previous cantilever beam case, the variation between the planar beam theory and the nonlinear extensible ribbon framework is negligible. The Young's modulus is changed to achieve different normalized stiffness and deformed configurations. Instead of using the normalized weight  $\gamma$  as the cantilever beam study, another parameter — normalized stiffness,  $\Gamma_g = 1/\gamma$ , is considered herein for the consistency with Raux et al. (2010).

From Fig. 6(A), it is found that the structure remains a circular shape and is close to its undeformed pattern for a relative large stiffness, e.g.,  $\Gamma_g = 2.30$ . When the structural rigidity decreases, the elastic ribbon would deform from a convex pattern to a concave shape. A touch down pattern is observed for a very small rigidity. Fig. 6(B) shows the dependence of relative height,  $H/2R$ , on the normalized stiffness,  $\Gamma_g$ , from

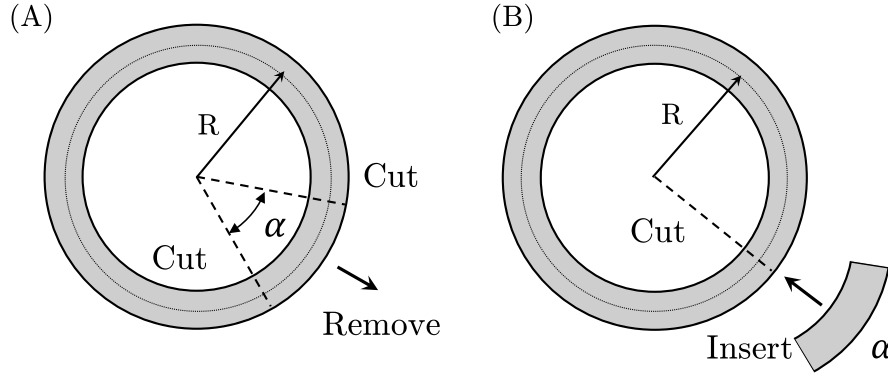


Fig. 7. Setup of two types of annular ribbons. (A): Overcurve. (B): Undercurve.

both numerical simulation (solid line) and experimental observation (circles). Refer to [Raux et al. \(2010\)](#) for the experimental data and related details. The excellent agreement indicates the accuracy of our discrete numerical approach.

### 3.3. Overcurve and undercurve in annular ribbons

An elastic ribbon with non-zero geodesic curvature,  $\bar{\kappa}_1(S) \neq 0$  is investigated in this subsection. Similarly, the first term in Eq. (5) needs to be modified as  $\sum_{i=1}^{N-2} \frac{1}{2} EI_1 (\kappa_{1,i} - \bar{\kappa}_{1,i})^2$ . [Kumar et al. \(2020\)](#) studied the mechanics of annular ribbons in a 2D plate approach. Here the 1D extensible ribbon framework is applied to the overcurve and undercurve in annular ribbons, as shown [Fig. 7](#).

The overcurve of annular ribbons is obtained if a piece of structure in size of  $\alpha$  is removed and the two ends are later connected, referring to [Fig. 7\(A\)](#) and [Fig. 8\(A1\)–\(A2\)](#). The geometric parameters used in both experimental study and numerical investigation are: ribbon radius  $R = 25$  mm, width  $w = 5$  mm, thickness  $b = 0.1$  mm. The arclength is  $l = (2\pi - \alpha)R$ , where  $\alpha$  is a variable. Young's modulus  $E = 1$  GPa, Poisson's ratio  $\nu = 0.2$ , and density  $\rho = 1000$  kg/m<sup>3</sup>. Dirichlet boundary condition is introduced to manually move the first two nodes,  $\{\mathbf{x}_0, \mathbf{x}_1\}$ , and the last two nodes,  $\{\mathbf{x}_{N-2}, \mathbf{x}_{N-1}\}$ , to guarantee the connection and the continuation, i.e.,  $\mathbf{x}_{N-1}$  is moved onto  $\mathbf{x}_1$  and  $\mathbf{x}_{N-2}$  is moved onto  $\mathbf{x}_0$ . The first twisting angle,  $\theta^0$ , is fixed to avoid a rigid body rotation. [Fig. 8\(A1\)](#) and [\(A2\)](#) show the deformed configurations of an overcurve annular ribbon from experiment and simulation, respectively. The supplementary angle between the normal vector of table,  $\mathbf{n}_{xy}$ , and one of the material director,  $\mathbf{m}_2$ , shown schematically in [Fig. 8\(A2\)](#), is used to quantitatively evaluate the deformed level in annular ribbons. The inclined angle,  $\psi$ , is plotted as a function of cut size  $\alpha$  in [Fig. 8\(A3\)](#), and a good match is found between the experiment, simulation, and analytical solution, where the analytical solution is derived based on pure geometric analysis

$$\psi = \arccos\left(\frac{2\pi - \alpha}{2\pi}\right). \quad (13)$$

Details are in [Appendix D](#).

In contrast to the overcurve case, undercurve is realized by adding a piece of ribbon into a compact  $2\pi$  sized annular ribbon. Due to its slenderness, the structure would experience a buckling instability and deform along its out-of-plane direction. Refer to [Fig. 7\(B\)](#) for the procedure and [Fig. 8\(B1\)](#) and [\(B2\)](#) for the deformed patterns from both experimental side and numerical approach. The physical parameters and the boundary conditions stay the same with the overcurve case. Similarly, the out-of-plane height,  $H$ , is adopted to quantitatively characterize the deformed configurations in undercurve annular ribbons. [Fig. 8\(B3\)](#) illustrates the relation between the normalized out-of-plane height,  $H/R$ , and the inserting angle,  $\alpha$  from both desktop experiments (circles) and discrete framework (solid line).

### 3.4. Möbius strips

The Möbius strip is a canonical example of the one-sided surface, which can be easily obtained by twisting one end of the circular strip through a  $\pi$  angle, as given in [Fig. 9](#). It involves the bending-twisting coupling in 1D slender objects. Two different colors (red and blue) are adopted to distinguish the inner and outer surfaces in an elastic ribbon for a better rendering effect. The amazing structure exists everywhere in natural environment, such as bio-molecule structures ([Han et al., 2010](#)), graphene ([Caetano et al., 2008](#); [Wang et al., 2010](#)), and optical polarization ([Bauer et al., 2015](#)). The deformation and topology of developable Möbius strip have already been theoretically and numerically investigated by [Starostin and Van Der Heijden \(2007\)](#) and [Shen et al. \(2015\)](#). [Kumar et al. \(2021\)](#) experimentally studied the surface curvature of the developable ribbon. Here, the mid-surface is assumed as stretchable but not developable. The physical parameters are set as: ribbon length  $l = 500$  mm, width  $w \in \{2, 10, 30\}$  mm, thickness  $b = 0.1$  mm, Poisson's ratio  $\nu = 0.4$ , resulting  $1/\kappa^* l \in \{0.25, 6.35, 57.15\}$ . As it is a purely geometry-depended problem, the material properties are randomly selected. Young's modulus is  $E = 1$  GPa and the density is  $\rho = 1000$  kg/m<sup>3</sup>. The first and last two nodes,  $\{\mathbf{x}_0, \mathbf{x}_1, \mathbf{x}_{N-2}, \mathbf{x}_{N-1}\}$ , are specified to keep the curvature continuation at the joint area. The first and last one twisting angle,  $\{\theta^0, \theta^{N-2}\}$ , are gradually increased (or decreased) to realize the twist at boundaries. The deformed configurations from the Kirchhoff rod model, extensible ribbon model, and Sadowsky ribbon model are presented in [Fig. 10\(A\)](#) and [\(B\)](#). As expected, the prediction from extensible ribbon framework is closer to linear rod model when the normalized curvature is small, and slowly approximates to the developable ribbon theory as  $1/\kappa^* l$  increases. The maximum (as well as minimum)  $z$  position evaluated from Sadowsky model is slightly larger than the prediction in linear rod theory. In [Fig. 10\(C\)](#) and [\(D\)](#), the variations of normalized bending curvature and twisting curvature along strip arclength,  $S$ , are presented from different energy functionals, and a similar trend can be observed meanwhile. It can be inferred that the twisting curvature at ribbon's midpoint derived from rod model is convex, while the data computed from Sadowsky theory shows an opposite trend. The slope is zero when a suitable normalized curvature is selected in the extensible ribbon framework, which again indicates its capacity to bridge the gap between the two classical theories. It should be noted that the inflection points in our numerical case are two boundary points, i.e.,  $S = 0$  and  $S = 1$ , where the curvatures are not continuous.

### 3.5. Lateral-torsional buckling of beams

In this subsection, another bending-twisting coupling problem, lateral-torsional buckling of beams, is focused on. Lateral-torsional buckling of beams is an important failure mode in civil engineering when

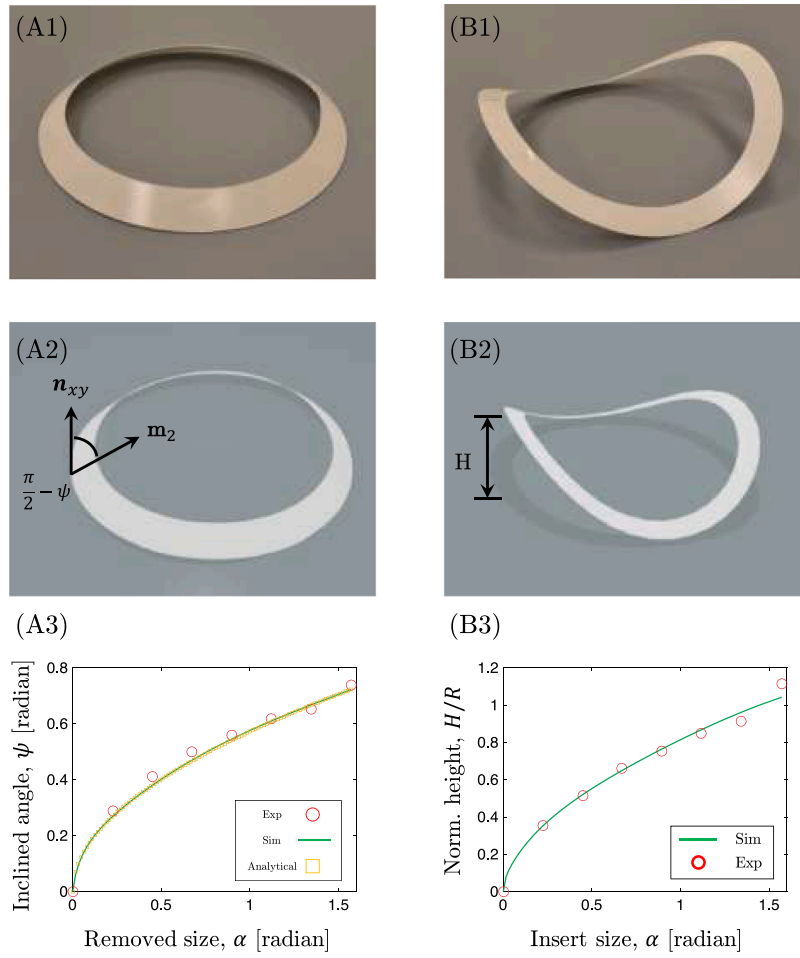


**Fig. 8.** (A1)–(A3): Overcurve of annular ribbons. (B1)–(B3): Undercurve of annular ribbons. (A1) and (B1): Desktop experiments. (A2) and (B2): Numerical renderings. (A3): Inclined angle,  $\psi$ , as a function of removed size,  $\alpha$ , in overcurve annular ribbons. (B3): Relative height,  $H/R$ , changes as the inserting size,  $\alpha$ , for undercurve annular ribbons.

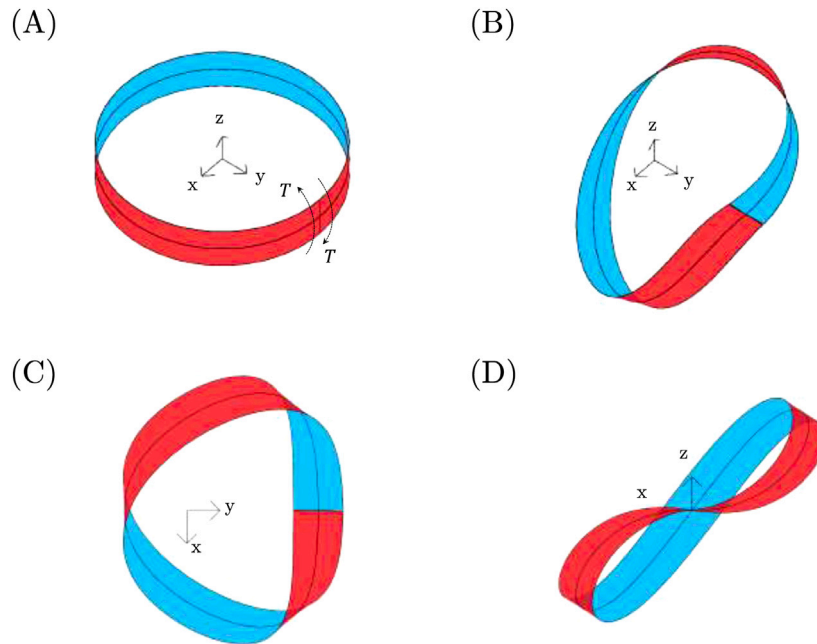


**Fig. 9.** (A): Numerical setup for Möbius strip. (B): 3D configuration for a deformed Möbius strip. (C): Top view of a deformed Möbius strip. (D): Front view of a deformed Möbius strip.



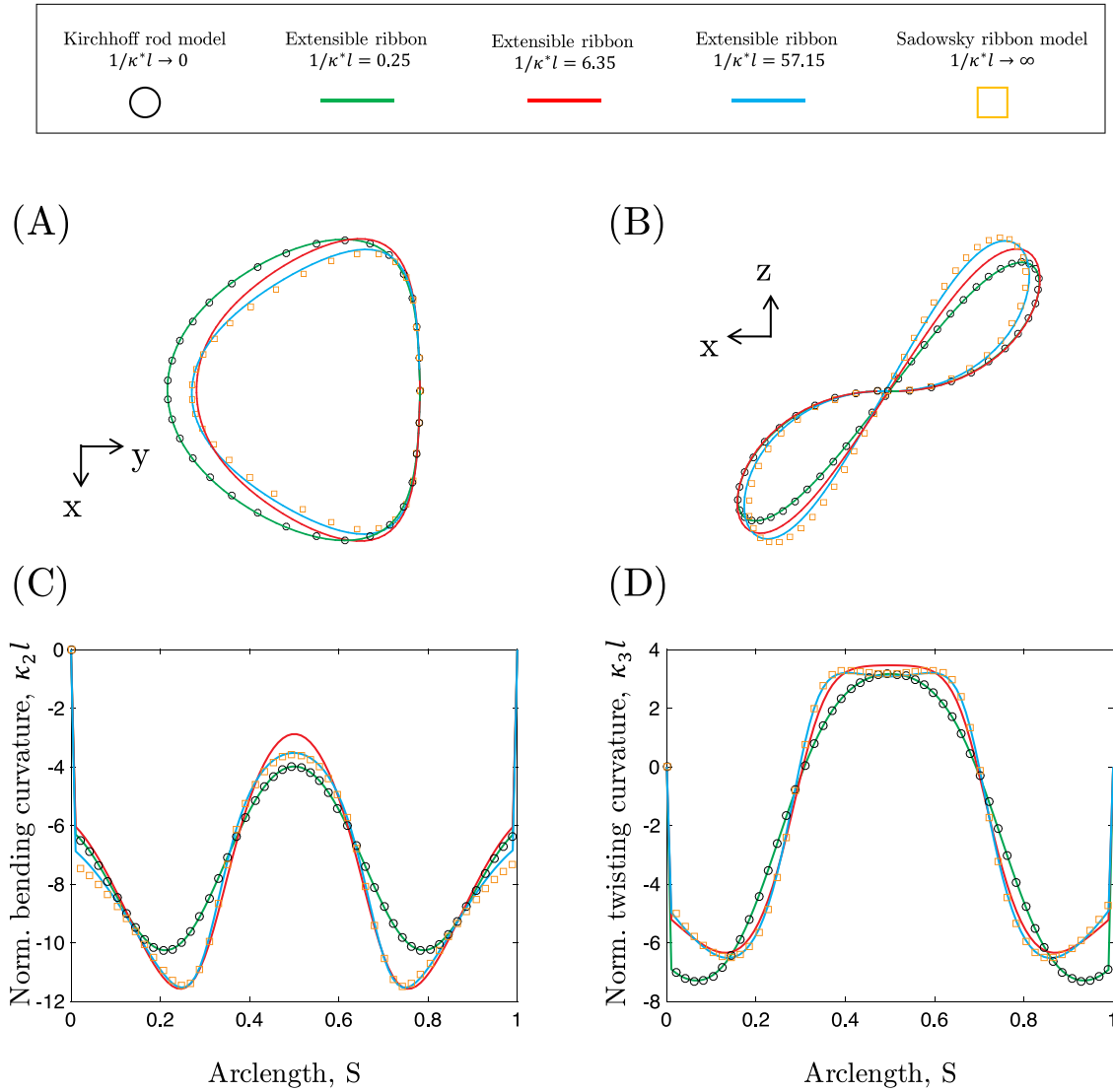


**Fig. 10.** (A) and (B): Top view and front view of Möbius strip centerlines computed from different models. (C) and (D): Variations of bending curvature and twisting curvature along the strip arclength,  $S$ , from different models.

the long steel beams carry important shear loads, and the investigation of lateral-torsional buckling can date back to 19th century. Recently, Romero et al. (2021) studied this problem through a simple 1D rod-based approach. In Audoly and Neukirch (2021), the nonlinear energy functional in Eq. (A.7) was derived and AUTO was used to solve the ODEs with associated boundary conditions through a continuous approach. Here, our established DDG-based approach is applied to revisit the lateral-torsional buckling problem. A clamped-free ribbon schematically shown in Fig. 11 would be stable and stay within a planar configuration when the gravity is moderate compared with its rigidity. However, a supercritical pitchfork bifurcation could appear once the external loading is beyond the threshold, such that the structure fails to keep its planar shape and will deform into a 3D pattern. For consistency, the same physical parameters in Audoly and Neukirch (2021) are configured: ribbon width  $w \in \{1.88, 5.10, 20.05\}$  mm, thickness  $b = 0.0925$  mm, Poisson's ratio  $\nu = 0.4$ , material property  $\sqrt{E/\rho} = 1820$  m/s (which is trivial for the equilibrium analysis). The ribbon length  $l$  is continuously changed to achieve different non-dimensional weights,  $\gamma = \frac{\rho w b g l^3}{E w b^3 / 12}$ , the scaling law of which stays the same as the previous cantilever beam case. The boundary conditions are also identical to the cantilever beam study, i.e., the first two nodes and the first twisting angle are fixed to achieve the clamped-free boundary conditions. The

relative tip displacement along the  $y$  axis is utilized to capture the deformed configurations of elastic ribbons.

In Fig. 12(A), the tip transverse deflection,  $d/l$ , is evaluated by changing the normalized weight,  $\gamma$ , with three different models: Kirchhoff rod model, the extensible ribbon framework, and Sadowsky theory. The critical weight that induces the supercritical bifurcation is  $\gamma_{\text{kirch}} = 15.4$  when the Kirchhoff rod model is applied, while the result obtained by ideal Sadowsky ribbon model is  $\gamma_{\text{sdw}} = 25.6$ , which are exactly the same as the analytical solution from linear bifurcation analysis, e.g.,  $\gamma_{\text{kirch}} = \frac{18.178}{\sqrt{1+\nu}}$  and  $\gamma_{\text{sdw}} = \frac{21.491}{1-\nu^2}$  (Audoly and Neukirch, 2021). The threshold value from the extensible ribbon model is close to the Kirchhoff rod theory, regardless of different ribbon geometries. The relations between the normalized length,  $l/L_{\text{eg}}$ , and the structural tip displacement,  $d/L_{\text{eg}}$ , are presented in Fig. 12(B). Here,  $L_{\text{eg}} = \left( \frac{E w b^3 / 12}{\rho w b g} \right)^{1/3}$  is the so-called elasto-gravitational length, which is used to analyze the relative ratio between the elastic bending energy and the gravitational potential. In both Fig. 12(A) and (B), it is found that the extensible ribbon framework is close to the Kirchhoff rod model when  $1/\kappa^*l$  is small, and gradually approximates to the Sadowsky theory as the normalized curvature increases. It should be noted that the data from our discrete numerical simulations are identical to the continuous

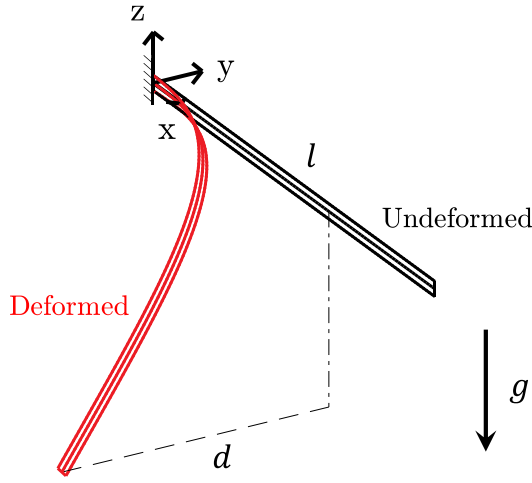


Fig. 11. Numerical setup for lateral-torsional buckling problem.

approach originally presented in Audoly and Neukirch (2021), in which the AUTO-based prediction has been validated against the experimental data and 2D shell-based finite element analysis. Refer to Fig. 4.4 in Audoly and Neukirch (2021) for details.

### 3.6. Shear induced bifurcation of pre-buckled ribbons

In this subsection, a shear induced supercritical pitchfork bifurcation in pre-buckled ribbons is explored with our proposed framework (Yu and Hanna, 2019; Huang et al., 2020b). An initial planar strip would experience buckling instability once the uniaxial loading exceeds a certain threshold, known as Euler's Elastica. In this case, the structure may undergo a supercritical pitchfork bifurcation when the transverse shear is introduced into the mechanical system (Yu and Hanna, 2019; Huang et al., 2020b, 2021a). As for this structure, the inflection points always occur along the ribbon's arclength. Herein, the inflection point refers to a location where the bending curvature changes its direction, and the prediction from ideal developable ribbon model (e.g., Sadowsky model) is discontinuous and singular, as it assumes the structural thickness is ideal zero and the in-plane stretching is totally forbidden. In the previous work, it was found that the 2D plate-based simulations could bridge the gap between the linear rod theory and developable Sadowsky framework (Huang et al., 2020b). According to Fig. 2, it reveals that the gap between the linear rod and the developable ribbon can also be fulfilled by the dimension-reduction-based 1D extensible ribbon approach.

The involved geometric parameters are configured as: ribbon length  $l = 300$  mm, width  $w \in \{2, 8, 20\}$  mm, thickness  $b = 0.1$  mm. The material parameters are chosen same to the previous case (with Young's modulus  $E = 1$  GPa, Poisson's ratio  $\nu = 0.0$ , and density  $\rho = 1000$  kg/m<sup>3</sup>). Accordingly,  $1/\kappa^*l \in \{0.46, 7.39, 46.19\}$ . The clamped-clamped boundary conditions are configured by constraining the first two nodes, first twisting angle, last two nodes, and the last twisting angle,  $\{\mathbf{x}_0, \theta^0, \mathbf{x}_1, \mathbf{x}_{N-2}, \theta^{N-2}, \mathbf{x}_{N-1}\}$ . Specifically, two twisting angles are always constrained as zeros, while the boundary nodes are manually moved to satisfy different uniaxial compression,  $\Delta l$ , and transverse shear,  $\Delta w$ .

In Fig. 13, the strip is first compressed by a prescribed distance,  $\Delta l/l = 0.5$ , leading to a buckling instability. Then, different patterns could be derived by enforcing a specified transverse shear,  $\Delta w$ . For instance, three patterns,  $U$ ,  $US$ , and  $S$  can be observed when the transverse displacements are  $\Delta w/l \in \{0.2, 0.4, 0.6\}$  respectively as illustrated in Fig. 14(A1)–(C1). Although the supercritical pitchfork bifurcation point that separates  $U$  and  $US$  diagrams is almost unchanged as long as

$l \gg w \gg h$  (Yu and Hanna, 2019; Huang et al., 2020b; Huang, 2021), it can be found that the curvature varies along the ribbon centerline when the normalized curvature  $1/\kappa^*l$  is changed, which is related to the ratio between  $l/w$  and  $w/h$  (Huang, 2021). As for a small value of the transverse shear, e.g.,  $\Delta w/l = 0.2$ , the configurations predicted by different numerical frameworks are almost the same as shown in Fig. 14(A1). However, the variations are no long negligible for a large value of the transverse shear, referring to Fig. 14(B1) and (C1). The variations of normalized bending and twisting curvatures along ribbon arclength are also given in Fig. 14. Even for small transverse shear, a significant mismatch could be found between the linear Kirchhoff rod model and developable Sadowsky framework. The curvatures predicted by the Kirchhoff model are continuous everywhere, while the results obtained by Sadowsky theory are singular at the inflection points, referring to the points at  $S = \{0.25, 0.75\}$  in case of  $\Delta w/l = 0.2$ . Also, similar to the previous scenarios, the presented discrete extensible ribbon simulation can fulfill the gap between the two classical models, i.e., on the one side, for small  $1/\kappa^*l$ , extensible ribbon model is almost identical to rod theory, and its curvatures are continuous; on the other side, the extensible ribbon model would slowly convergent to Sadowsky framework when  $1/\kappa^*l$  becomes larger and larger. It should be noted that the ideal Sadowsky model fails to capture the supercritical pitchfork bifurcation automatically and its prediction always remains within  $U$  patterns if no man-made interventions are introduced, the reason of which is inferred as the energy barrier at the inflection points (Huang et al., 2020b). Refer to the Appendix A of Huang et al. (2020b) for a solution to tackle this issue with an optimization-based numerical simulation.

### 3.7. Twist-induced snapping in bent ribbons

Another example is chosen as the twist-induced snapping in bent ribbons that was investigated by Sano and Wada (2019). A naturally straight strip would form an arc with its two ends held (Fig. 15). When its two ends are rotated along the same direction, the strip may deflect, then recoil, and return to its arc-like configuration after a snap-through flip (Sano and Wada, 2019). This type of snap-through behavior can only be observed for narrow ribbons while a fold pattern occurs for ribbons with a larger width. These two representative nonlinear processes, flip and fold, are given in Fig. 16(A) and (B), respectively. Similar to the case of shear induced supercritical pitchfork bifurcation in pre-buckled ribbons, the clamped-clamped boundary conditions in this setup could also be achieved by constraining 14 DOFs,  $\{\mathbf{x}_0, \theta^0, \mathbf{x}_1, \mathbf{x}_{N-2}, \theta^{N-2}, \mathbf{x}_{N-1}\}$ . Difference exists in that the four boundary nodes are fully fixed and the external actuations,  $\phi$ , are applied on the two twisting angles,  $\{\theta^0, \theta^{N-2}\}$ . The physical parameters are identically selected as that in Sano and Wada (2019): ribbon radius  $R = l/\pi = 108$  mm, width  $w \in \{8, 15\}$  mm, thickness  $b = 0.2$  mm, Poisson's ratio  $\nu = 0.3$ , Young's modulus  $E = 1$  GPa, and density  $\rho = 1000$  kg/m<sup>3</sup>. The midpoint position,  $\mathbf{x}_{\text{mid}} \equiv [\mathbf{x}_{\text{mid}}, \mathbf{y}_{\text{mid}}, \mathbf{z}_{\text{mid}}]$  is used to quantify the deformed configuration in elastic ribbons.

In Sano and Wada (2019), experimental and analytical approaches are combined, which found that the ribbon would flip when  $\frac{4.84}{\pi} bl/w^2 \lesssim 1$ , and would fold if  $\frac{4.84}{\pi} bl/w^2 \gtrsim 1$ . Regardless of the geometric properties in elastic ribbons, the normalized curvatures are assumed as zeros in anisotropic rod model,  $1/\kappa^*l \sim bl/w^2 \rightarrow 0$ , and its predicted elastic ribbons are always flip; However, the normalized curvatures in Sadowsky theory are always set to be infinite,  $1/\kappa^*l \sim bl/w^2 \rightarrow \infty$ . As a result, its predicted elastic ribbons are always fold. Neither Kirchhoff rod theory nor Sadowsky model could comprehensively describe the nonlinear mechanics in this special 1D object, which could be covered by the proposed extensible ribbon model. For small normalized curvatures,  $1/\kappa^*l$ , the in-plane stretching energy,  $E_{\text{str}}$ , in Eq. (A.7) is trivial compared with the elastic bending and twisting energies,  $E_{\text{Kirch}}$ , resulting in a flip response similar to the linear rod simulation. However, the in-plane stretching energy,  $E_{\text{str}}$ , becomes more and

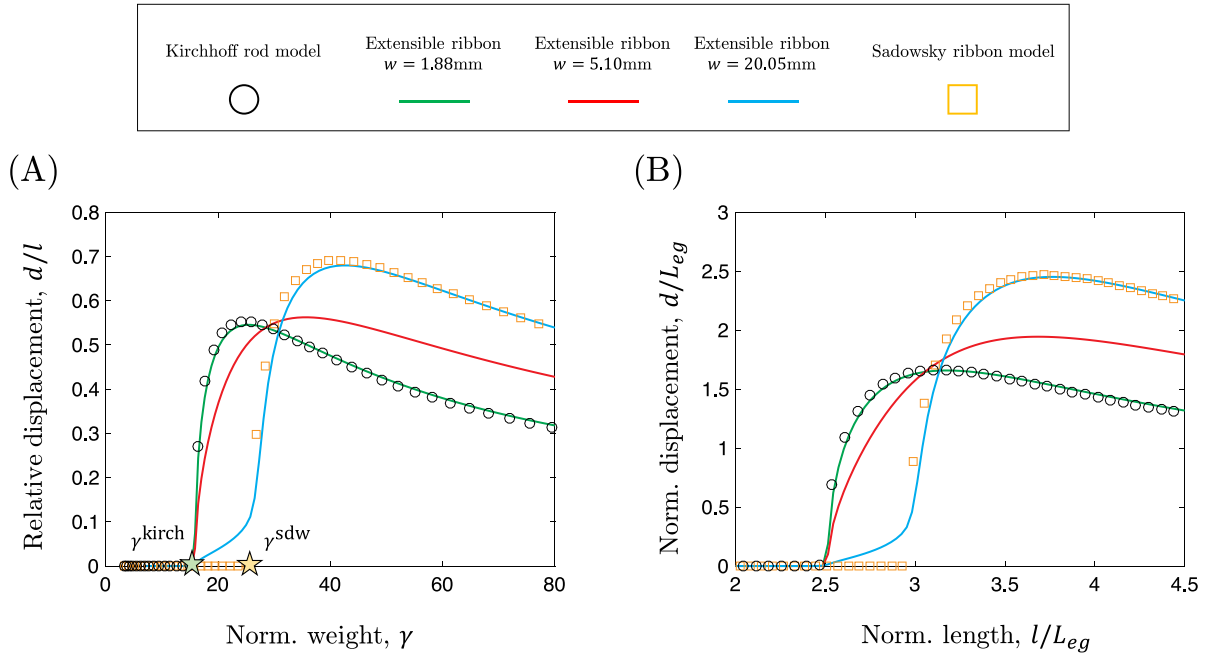


Fig. 12. Numerical solutions for the lateral-torsional buckling problem. (A): Variations of relative deflection,  $d/l$ , with the normalized weight,  $\gamma$ . (B): Plots of the normalized beam tip displacement,  $d/L_{eg}$ , versus normalized length,  $l/L_{eg}$ .

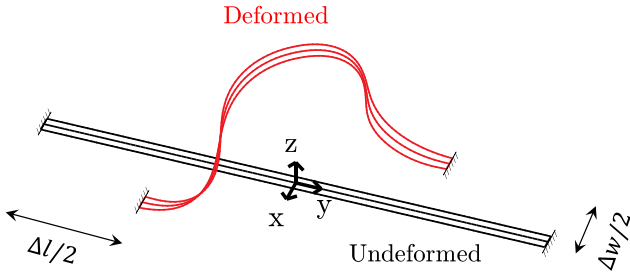


Fig. 13. Numerical setup for the shear induced supercritical pitchfork bifurcation in a pre-buckled ribbon.

more predominant than the Kirchhoff energy functional,  $E_{\text{Kirch}}$ , when the normalized curvature,  $1/\kappa^*l$ , is large enough. As a result, a fold pattern close to the Sadowsky model would be observed. To make a quantitative comparison, the variations of relative midpoint position,  $y_{\text{mid}}/R$ , with respect to the actuating angle,  $\phi$ , is shown in Fig. 17. Both flip and fold responses could be observed in our discrete simulation. Excellent agreement between the results in (Sano and Wada, 2019) and our numerical simulation demonstrates accuracy of the proposed DDG-based framework.

To demonstrate the correctness and accuracy of our numerical framework, the convergent study is presented in Appendix E. The treatment of numerical issue when  $EA \gg EI_2$  (or poor Hessian matrix) is detailed in Appendix F.

#### 4. Conclusion

A DDG-based numerical simulation was developed to explore the geometrically nonlinear mechanics in extensible ribbons, which fulfilled the gap between two traditional 1D theories, Kirchhoff rod model and Sadowsky ribbon model. With the energy functional that was originally proposed by Sano and Wada (2019) and Audoly and Neukirch (2021), a cross section-depended parameter was introduced to allow a finite in-plane stretching in ribbon's mid-surface, and meanwhile avoid the singularity at structural inflection points. In the numerical

framework, the 1D energy functional was discretized into a mass-spring system, in a manner similar to the well-known DER method. Relevant constraints, such as the inextensibility of strip centerline and the bending around strip surface normal, were transformed into several discrete potential energies and established through penalty-based method. The total potentials were separated into two unrelated parts — the material-depended part and the geometry-depended part, based on which the gradient associated with internal elastic force and the Hessian associated with Jacobian matrix were formulated. A group of discrete equations of motion for extensible ribbons were solved via the first-order implicit Euler method with its numerical stability and unconditional convergence involved in. Its equilibrium configuration was obtained through dynamic relaxation method. It should be noted that our numerical approach was a fully implicit framework. Several typical examples were analyzed and discussed to compare the proposed method, the linear Kirchhoff rod model and developable Sadowsky ribbon theory, whose results demonstrated the advantage of our DDG-based extensible ribbon simulator.

It is noteworthy that the strain gradient terms in energy functional are ignored in this paper. The assumption is valid as long as the object is slender, e.g.,  $l \gg w$ . However, it becomes no longer applicable when its length and width are in the same order of magnitude, where the role of strain gradient would be predominant and could not be disregarded (Audoly and Neukirch, 2021; Lestringant and Audoly, 2020; Audoly and Lestringant, 2021). The classical Wunderlich ribbon functional considered the strain gradient effect but it was still under an assumption that the surface was developable, which was thus unable to capture the variations when the ribbon thickness changed. What is more, its prediction was singular at the inflection points, similar to the Sadowsky ribbon theory. Future works should be focused on the formulation of a general 1D theory of the undevelopable ribbons, with the strain gradient effect considered. Application of a data-driven approach to this dimension reduced problem may provide a valid solution. For example, a neural network can be trained to model the ribbon-like structures with the dataset extracted from a 2D plate simulation. A general 1D numerical framework will also be of value if it is able to capture the localization phenomena of an elastic strip that has a non-rectangular cross-section (Brunetti et al., 2020).

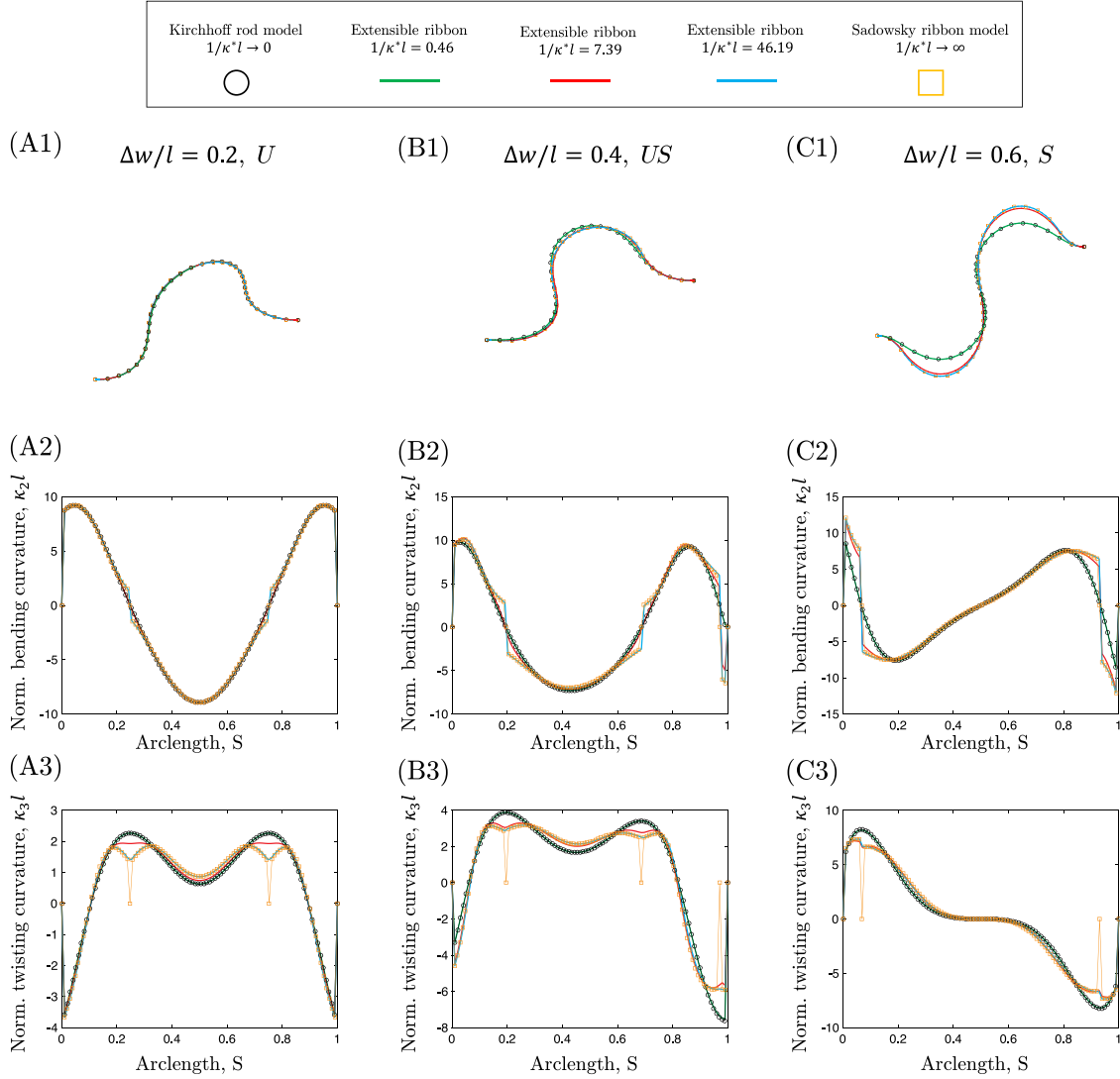


**Fig. 14.** Plots of elastic ribbons with different boundary conditions and different patterns: (A1)–(A3)  $\Delta w/l = 0.2, U$  pattern. (B1)–(B3)  $\Delta w/l = 0.4, US$  pattern. (C1)–(C3)  $\Delta w/l = 0.6, S$  pattern. (A1)–(C1) Strip centerline in deformed configurations. (A2)–(C2) Variations of bending curvatures,  $\kappa_2 l$ , along ribbon arclength. (A3)–(C3) Variations of twisting curvatures,  $\kappa_3 l$ , along ribbon arclength.

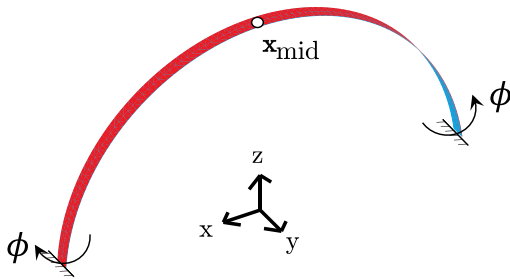


**Fig. 15.** Numerical setup for the twist-induced snapping in a bent ribbon.

### Declaration of competing interest

The authors declare that they have no known competing financial interests or personal relationships that could have appeared to influence the work reported in this paper.

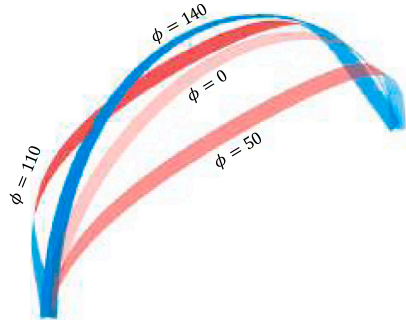
### Acknowledgments

This work was supported by the Natural Science Foundation of Jiangsu Province (No. BK20210233), the Open Foundation of the State Key Laboratory of Fluid Power and Mechatronic Systems (No. GZKF-202113), and the Jiangsu Planned Projects for Postdoctoral Research Funds (2021K230B).

### Appendix A. Ribbon model

In this appendix, the continuous model of extensible ribbons will be revisited, which was originally proposed by Audoly and Neukirch (2021). The structure considered herein is of length  $l$ , width  $w$ , thickness  $b$ , and the material is isotropic, linearly elastic. The Young's modulus is represented by  $E$  and Poisson's ratio by  $\nu$ . In the reference configuration, the longitudinal coordinate and the transverse coordinate are denoted by  $S$  and  $T$ , respectively. Assuming the strip centerline is inextensible, the same  $S$  is used to denote the longitudinal coordinates in both reference and deformed configurations.

(A)

Flip,  $(b, w, R) = (0.2, 8, 108)$ 

(B)

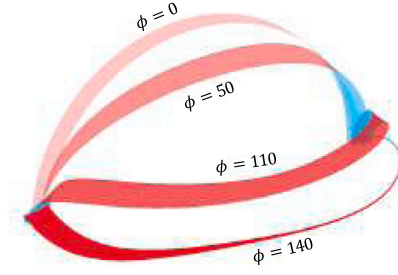
Fold,  $(b, w, R) = (0.2, 15, 108)$ 

Fig. 16. Two representative mechanical responses of elastic ribbons in different shapes. (A): Flip,  $(b, w, R) = (0.2, 8, 108)$  mm. (B): Fold,  $(b, w, R) = (0.2, 15, 108)$  mm.

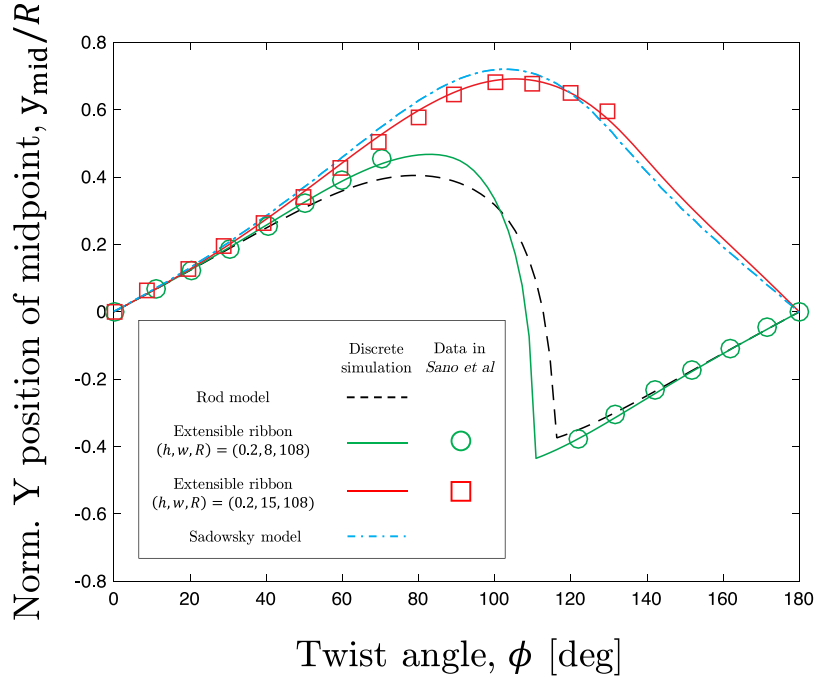


Fig. 17. Normalized midpoint position,  $y_{\text{mid}}/R$ , versus twisting angle,  $\phi$ , from different numerical frameworks: Kirchhoff rod model, extensible ribbon formulation, and Sadowsky ribbon theory. Note that the symbolic used for validation is from Sano and Wada (2019).

As shown in Fig. A.18, the 1D strip is parameterized by a space curve called centerline,  $\mathbf{r}(S)$ , together with a material frame,  $\{\mathbf{m}_1(S), \mathbf{m}_2(S), \mathbf{m}_3(S)\}$ , where  $\mathbf{m}_3(S) = \mathbf{r}'(S)/|\mathbf{r}'(S)|$  is the tangential direction,  $\mathbf{m}_1(S)$  is the surface normal, and  $\mathbf{m}_2(S) = \mathbf{m}_3(S) \times \mathbf{m}_1(S)$  is the edge vector. It should be noted that the material frame is orthonormal, i.e.,  $\forall S \mathbf{m}_\alpha \cdot \mathbf{m}_\beta = \delta_{\alpha\beta}$ . Herein  $\delta_{\alpha\beta}$  is the Kronecker delta and  $\alpha$  (and  $\beta$ ) runs by default along all directions of space,  $\alpha, \beta \in \{1, 2, 3\}$ .

The uniaxial strain of the centerline is given by

$$\epsilon(S) = |\mathbf{r}'(S)| - 1, \quad (\text{A.1})$$

and its rotation gradient is formulated as

$$\mathbf{m}'_\alpha = \boldsymbol{\omega} \times \mathbf{m}_\alpha, \quad (\text{A.2a})$$

$$\boldsymbol{\omega} = \kappa_\alpha \mathbf{m}_\alpha, \quad (\text{A.2b})$$

where  $\boldsymbol{\omega}$  is the Darboux vector,  $\kappa_1(S)$  is the in-plane bending curvature,  $\kappa_2(S)$  is the out-of-plane bending curvature, and  $\kappa_3(S)$  is the twisting curvature. Overall, the macroscopic strain for 1D structures consists of the elastic stretching strain in Eq. (A.1) and elastic bending and twisting curvatures in Eq. (A.2). As we mainly focus on the out-of-plane bending deformations and ignore the high-tension case, the stretching of its centerline and the bending around  $\mathbf{m}_1$  direction need to be constrained. Thus, we assume the elastic energy is only a function of  $\kappa_2(S)$  and  $\kappa_3(S)$ , while  $\epsilon(S)$  and  $\kappa_1(S)$  are totally forbidden as described by Eq. (A.3).

$$\forall S \begin{cases} \epsilon(S) = 0 \\ \kappa_1(S) = 0. \end{cases} \quad (\text{A.3})$$

Notice that the extensible ribbon in the current investigation means the ribbon mid-surface is extensible, which is different from the well-established developable ribbon model (Sadowsky model or Wunderlich



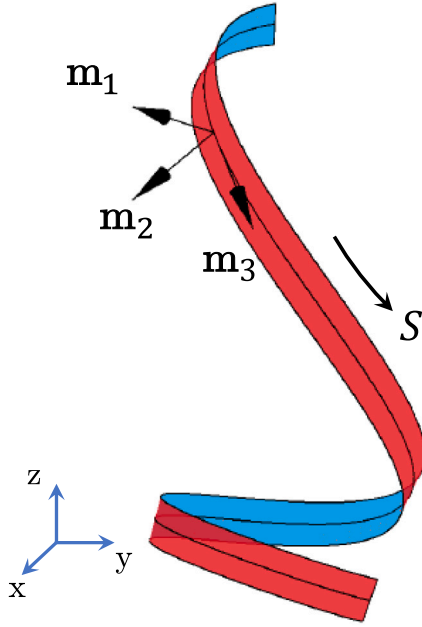


Fig. A.18. Configuration of a narrow strip.

model); however, the ribbon centerline is inextensible, as mentioned above.

Based on the derived macroscopic strains, the elastic energies for 1D extensible ribbon are formulated next. The energy functional can be derived from a 2D plate-based model through a dimensional reduction procedure. As the object considered here always stays within the slender regime, its length is much larger than the other dimensions and the strain gradient effect is ignored. The total potential energy can be written as Eq. (A.4) (Audoly and Neukirch, 2021):

$$\begin{aligned} \Phi &= \int_0^l W(\kappa_2(S), \kappa_3(S)) dS \\ &= \int_0^l \left[ \frac{1}{2} \frac{Ewb^3}{12} \kappa_2^2 + \frac{1}{2} \frac{Ewb^3}{6(1+\nu)} \kappa_3^2 + \frac{1}{2} \frac{Ebw^5}{2} (\nu \kappa_2^2 + \kappa_3^2)^2 \phi\left(\frac{\kappa_2}{\kappa^*}\right) \right] dS, \end{aligned} \quad (\text{A.4})$$

where  $\kappa^*$  is the characteristic curvature strain (Audoly and Neukirch, 2021),

$$\kappa^* = \frac{1}{[12(1-\nu)]^{1/2}} \frac{b}{w^2}, \quad (\text{A.5})$$

and  $\phi(x)$  is a numerical function (Audoly and Neukirch, 2021),

$$\phi(x) = \frac{4}{\nu^2} \left[ \frac{1}{2} - \frac{\cosh \sqrt{\frac{|x|}{2}} - \cos \sqrt{\frac{|x|}{2}}}{\sqrt{\frac{|x|}{2}} \left( \sinh \sqrt{\frac{|x|}{2}} + \sin \sqrt{\frac{|x|}{2}} \right)} \right]. \quad (\text{A.6})$$

The complex energy functional in Eq. (A.4) can be simplified to Eq. (A.7) without notable errors introduced (Sano and Wada, 2019; Audoly and Neukirch, 2021),

$$\Phi_{\text{sim}} = \int_0^l \left[ \frac{1}{2} \frac{Ewb^3}{12} \kappa_2^2 + \frac{1}{2} \frac{Ewb^3}{6(1+\nu)} \kappa_3^2 + \frac{1}{2} \frac{Ewb^3}{12(1-\nu^2)} \frac{(\nu \kappa_2^2 + \kappa_3^2)^2}{\frac{60}{1-\nu^2} \frac{b^2}{w^4} + \kappa_2^2} \right] dS. \quad (\text{A.7})$$

Here, the first two terms are denoted by  $E_{\text{Kirch}}$  and the last term by  $E_{\text{str}}$ . The energy functional formulated in Eq. (A.4) (and Eq. (A.7)) can bridge the gap between classical Kirchhoff rod model and developable Sadowsky ribbon model (Sano and Wada, 2019; Audoly and Neukirch,

2021). On the one hand, this non-linear 1D energy functional would become closer to the classical Kirchhoff rod model when the structural curvatures are much smaller compared with the characteristic curvature,  $|\kappa_\alpha| \ll \kappa^*$ ,

$$\Phi \sim \Phi_{\text{Kirchhoff}} = \int_0^l \left[ \frac{1}{2} \frac{Ewb^3}{12} \kappa_2^2 + \frac{1}{2} \frac{Ewb^3}{6(1+\nu)} \kappa_3^2 \right] dS; \quad (\text{A.8})$$

On the other hand, the proposed energy functional would approximate to the developable Sadowsky ribbon model if the structural curvature becomes much larger than the characteristic curvature,  $|\kappa_\alpha| \gg \kappa^*$ ,

$$\Phi \sim \Phi_{\text{Sadowsky}} = \int_0^l \left[ \frac{1}{2} \frac{Ewb^3}{12(1-\nu^2)} \frac{(\kappa_2^2 + \kappa_3^2)^2}{\kappa_2^2} \right] dS. \quad (\text{A.9})$$

It indicates by Eqs. (A.4) and (A.7) that a relative difference of the bending stiffness for an elastic strip in pure bending case (where  $\kappa_3(S)$  is zero), exists as  $\left(\frac{1}{1-\nu^2} - 1\right)$  between the small strain regime and the large strain regime, which is equivalent to the Shield's model (Shield, 1992; Audoly and Neukirch, 2021).

The governing equations for extensible ribbons is derived through a variational approach in a manner similar to the standard rod model.

*Kinematic equations:*

$$\mathbf{r}'(S) = \mathbf{m}_3(S) \quad (\text{A.10a})$$

$$\mathbf{m}_\alpha(S) \cdot \mathbf{m}_\beta(S) = \delta_{\alpha\beta} \quad (\text{A.10b})$$

$$\mathbf{m}'_\alpha(S) = \boldsymbol{\omega}(S) \times \mathbf{m}_\alpha(S) \quad (\text{A.10c})$$

$$\boldsymbol{\omega}(S) = \kappa_2(S) \mathbf{m}_2(S) + \kappa_3(S) \mathbf{m}_3(S). \quad (\text{A.10d})$$

*Equilibrium equations:*

$$\mathbf{N}'(S) + \mathbf{f}(S) = \mathbf{0} \quad (\text{A.11a})$$

$$\mathbf{M}'(S) + \mathbf{m}_3(S) \times \mathbf{N}'(S) = \mathbf{0}, \quad (\text{A.11b})$$

where  $\mathbf{f}(S)$  is the external force density,  $\mathbf{N}(S)$  is the internal force, and  $\mathbf{M}(S)$  is the internal moment.

*Constitutive equations:*

$$\mathbf{M}_2(S) = \frac{\partial W}{\partial \kappa_2}(\kappa_2(S), \kappa_3(S)) \quad (\text{A.12a})$$

$$\mathbf{M}_3(S) = \frac{\partial W}{\partial \kappa_3}(\kappa_2(S), \kappa_3(S)), \quad (\text{A.12b})$$

where  $\mathbf{M}_2(S)$  and  $\mathbf{M}_3(S)$  are the components of internal moment,  $\mathbf{M}(S) = \mathbf{M}_2(S) \mathbf{m}_2(S) + \mathbf{M}_3(S) \mathbf{m}_3(S)$ , and  $W$  is the strain energy density in Eq. (A.4) (and Eq. (A.7)). It should be noted that the bending moment around forbidden direction,  $\mathbf{M}_1(S)$ , acts like a penalty parameter to ensure  $\kappa_1(S) \equiv 0$ , and the internal force,  $\mathbf{N}(S)$ , also performs as a penalty parameter to establish  $\epsilon(S) \equiv 0$ .

Overall, a BVP is well defined and the equilibrium configuration of a narrow ribbon can be derived by solving the differential equations and the associated boundary conditions.

## Appendix B. First variation of macroscopic strains

In this appendix, we review the first variation of macroscopic strains,  $\{\epsilon^i, \kappa_{1,i}, \kappa_{2,i}, \kappa_{3,i}\}$ . First of all, we introduce

$$\begin{aligned} \bar{\mathbf{m}}_1 &= \frac{(\mathbf{m}_1^{i-1} + \mathbf{m}_1^i)}{1 + \mathbf{m}_3^{i-1} \cdot \mathbf{m}_3^i} \\ \bar{\mathbf{m}}_2 &= \frac{(\mathbf{m}_2^{i-1} + \mathbf{m}_2^i)}{1 + \mathbf{m}_3^{i-1} \cdot \mathbf{m}_3^i} \\ \bar{\mathbf{m}}_3 &= \frac{(\mathbf{m}_3^{i-1} + \mathbf{m}_3^i)}{1 + \mathbf{m}_3^{i-1} \cdot \mathbf{m}_3^i}, \end{aligned} \quad (\text{B.1})$$

and designate the space gradient

$$\begin{aligned}\nabla_{i-1}() &= \frac{\partial()}{\partial \mathbf{e}^{i-1}} \\ \nabla_i() &= \frac{\partial()}{\partial \mathbf{e}^i}.\end{aligned}\quad (\text{B.2})$$

The gradient of uniaxial strain associated with the  $i$ th edge in Eq. (1) is computed as

$$\nabla_i(\epsilon^i) = \frac{1}{|\mathbf{e}^i|} \mathbf{m}_3^i. \quad (\text{B.3})$$

Next, the gradient of bending curvature in Eq. (3) takes the form

$$\begin{aligned}\nabla_{i-1}(\kappa_{1,i}) &= \frac{1}{|\mathbf{e}^{i-1}|} (-\kappa_{1,i} \tilde{\mathbf{m}}_3 + \mathbf{m}_3^i \times \tilde{\mathbf{m}}_2) \\ \nabla_i(\kappa_{1,i}) &= \frac{1}{|\mathbf{e}^i|} (-\kappa_{1,i} \tilde{\mathbf{m}}_3 - \mathbf{m}_3^{i-1} \times \tilde{\mathbf{m}}_2),\end{aligned}\quad (\text{B.4})$$

and similarly for  $\kappa_{2,i}$ . Finally, the gradient of twisting strain in Eq. (4) is

$$\begin{aligned}\nabla_{i-1}(\kappa_{3,i}) &= \frac{(\kappa \mathbf{b})_i}{2|\mathbf{e}^{i-1}|} \\ \nabla_i(\kappa_{3,i}) &= \frac{(\kappa \mathbf{b})_i}{2|\mathbf{e}^i|}.\end{aligned}\quad (\text{B.5})$$

The gradient of elastic energy with respect to the twisting angle,  $\theta^i$ , can be trivially computed.

### Appendix C. Second variation of macroscopic strains

In this appendix, we review the second variation of macroscopic strains. The second variation is denoted as

$$\begin{aligned}\nabla_{i-1}^2() &= \frac{\partial^2()}{\partial (\mathbf{e}^{i-1})^2} \\ \nabla_i^2() &= \frac{\partial^2()}{\partial (\mathbf{e}^i)^2} \\ \nabla_{i-1} \nabla_i() &= \frac{\partial^2()}{\partial \mathbf{e}^{i-1} \partial \mathbf{e}^i}.\end{aligned}\quad (\text{C.1})$$

The second variation of uniaxial strain  $\epsilon^i$  is

$$\nabla_i^2(\epsilon^i) = \frac{1}{|\mathbf{e}^i|} \frac{(\mathbb{I}_3 - \mathbf{m}_3^i \otimes \mathbf{m}_3^i)}{|\mathbf{e}^i|}, \quad (\text{C.2})$$

where  $\mathbb{I}_3$  is a  $3 \times 3$  identity matrix. The second variations of material curvatures are given by:

$$\begin{aligned}\nabla_{i-1}^2(\kappa_{1,i}) &= \frac{1}{|\mathbf{e}^{i-1}|^2} [2\kappa_{1,i} \tilde{\mathbf{m}}_3 \otimes \tilde{\mathbf{m}}_3 - (\mathbf{m}_3^i \times \tilde{\mathbf{m}}_2) \otimes \tilde{\mathbf{m}}_3 - \tilde{\mathbf{m}}_3 \otimes (\mathbf{m}_3^i \times \tilde{\mathbf{m}}_2)] \\ &\quad - \frac{\kappa_{1,i}}{(1 + \mathbf{m}_3^{i-1} \cdot \mathbf{m}_3^i) |\mathbf{e}^{i-1}|^2} (\mathbb{I}_3 - \mathbf{m}_3^{i-1} \otimes \mathbf{m}_3^{i-1}) \\ &\quad + \frac{1}{4|\mathbf{e}^{i-1}|^2} [(\kappa \mathbf{b})_i \otimes \mathbf{m}_2^{i-1} + \mathbf{m}_2^{i-1} \otimes (\kappa \mathbf{b})_i], \\ \nabla_i^2(\kappa_{1,i}) &= \frac{1}{|\mathbf{e}^i|^2} [2\kappa_{1,i} \tilde{\mathbf{m}}_3 \otimes \tilde{\mathbf{m}}_3 + (\mathbf{m}_3^{i-1} \times \tilde{\mathbf{m}}_2) \otimes \tilde{\mathbf{m}}_3 + \tilde{\mathbf{m}}_3 \otimes (\mathbf{m}_3^{i-1} \times \tilde{\mathbf{m}}_2)] \\ &\quad - \frac{\kappa_{1,i}}{(1 + \mathbf{m}_3^{i-1} \cdot \mathbf{m}_3^i) |\mathbf{e}^i|^2} (\mathbb{I}_3 - \mathbf{m}_3^i \otimes \mathbf{m}_3^i) \\ &\quad + \frac{1}{4|\mathbf{e}^i|^2} [(\kappa \mathbf{b})_i \otimes \mathbf{m}_2^i + \mathbf{m}_2^i \otimes (\kappa \mathbf{b})_i], \\ \nabla_{i-1} \nabla_i(\kappa_{1,i}) &= [\nabla_i \nabla_{i-1}(\kappa_{1,i})]^T = \\ &\quad - \frac{\kappa_{1,i}}{(1 + \mathbf{m}_3^{i-1} \cdot \mathbf{m}_3^i) |\mathbf{e}^{i-1}| |\mathbf{e}^i|} (\mathbb{I}_3 + \mathbf{m}_3^{i-1} \otimes \mathbf{m}_3^i) \\ &\quad + \frac{2\kappa_{1,i} \tilde{\mathbf{m}}_3 \otimes \tilde{\mathbf{m}}_3 - (\mathbf{m}_3^i \times \tilde{\mathbf{m}}_2) \otimes \tilde{\mathbf{m}}_3 + \tilde{\mathbf{m}}_3 \otimes (\mathbf{m}_3^{i-1} \times \tilde{\mathbf{m}}_2) - \tilde{\mathbf{m}}_2 \otimes \tilde{\mathbf{m}}_2}{|\mathbf{e}^{i-1}| |\mathbf{e}^i|},\end{aligned}\quad (\text{C.3})$$

and it is similar for  $\kappa_{2,i}$ . Note that  $\otimes$  is the tensor product. The second variations of twist are

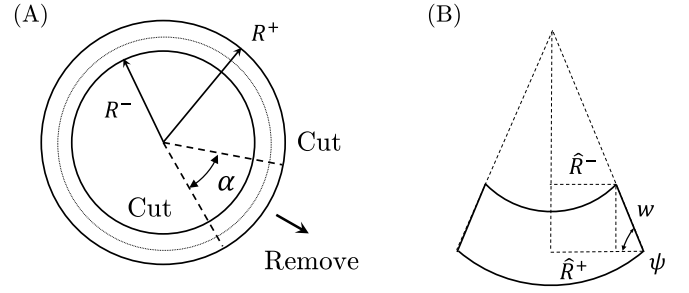


Fig. D.19. (A): Setup of an overcurve annular ribbon. (B): Deformed configuration of an overcurve annular ribbon.

$$\begin{aligned}\nabla_{i-1}^2(\kappa_{3,i}) &= -\frac{1}{4|\mathbf{e}^{i-1}|^2} [(\kappa \mathbf{b})_i \otimes (\mathbf{m}_3^{i-1} + \tilde{\mathbf{m}}_3) + (\mathbf{m}_3^{i-1} + \tilde{\mathbf{m}}_3) \otimes (\kappa \mathbf{b})_i], \\ \nabla_i^2(\kappa_{3,i}) &= -\frac{1}{4|\mathbf{e}^i|^2} [(\kappa \mathbf{b})_i \otimes (\mathbf{m}_3^i + \tilde{\mathbf{m}}_3) + (\mathbf{m}_3^i + \tilde{\mathbf{m}}_3) \otimes (\kappa \mathbf{b})_i], \\ \nabla_{i-1} \nabla_i(\kappa_{3,i}) &= [\nabla_i \nabla_{i-1}(\kappa_{3,i})]^T \\ &= \frac{1}{2|\mathbf{e}^{i-1}| |\mathbf{e}^i|} \left[ \frac{2}{1 + \mathbf{m}_3^{i-1} \cdot \mathbf{m}_3^i} (\mathbf{m}_3^{i-1} \otimes \mathbf{m}_3^{i-1}) - (\kappa \mathbf{b})_i \otimes \tilde{\mathbf{m}}_3 \right].\end{aligned}\quad (\text{C.4})$$

### Appendix D. Analytical solution for overcurve annular ribbon

In this appendix, we derive the analytical solution for overcurve annular ribbon. The setup is in Fig. D.19(A). The deformed inner radius is

$$\hat{R}^- = \frac{2\pi - \alpha}{2\pi} (R - \frac{w}{2}), \quad (\text{D.1})$$

and the deformed outer radius is

$$\hat{R}^+ = \frac{2\pi - \alpha}{2\pi} (R + \frac{w}{2}), \quad (\text{D.2})$$

and, referring to Fig. D.19(B), the inclined angle is given by

$$\cos \psi = \frac{\hat{R}^+ - \hat{R}^-}{w} = \frac{2\pi - \alpha}{2\pi}. \quad (\text{D.3})$$

### Appendix E. Convergent study

In this appendix, four cases are used to show the convergence of our numerical framework: (1) Cantilever beam; (2) Lateral-torsional buckling of beams; (3) Shear induced bifurcation of pre-buckled ribbons; and (4) Twist-induced snapping in bent ribbons. The physical parameters are: (1): ribbon length  $l = 1000$  mm, width  $w = 100$  mm, thickness  $b = 1$  mm, Young's modulus  $E = 1$  GPa, Poisson's ratio  $\nu = 0.4$ , density  $\rho = 1000$  kg/m<sup>3</sup>, and gravity  $g = 10$  m/s<sup>2</sup>; (2): ribbon length  $l = 150$  mm, width  $w = 20.05$  mm, thickness  $b = 0.0925$  mm, Poisson's ratio  $\nu = 0.4$ , material property  $\sqrt{E/\rho} = 1820$  m/s, and gravity  $g = 10$  m/s<sup>2</sup>; (3): ribbon length  $l = 300$  mm, width  $w = 8$  mm, thickness  $b = 0.1$  mm, Young's modulus  $E = 1$  GPa, Poisson's ratio  $\nu = 0.0$ , density  $\rho = 1000$  kg/m<sup>3</sup>, input compression  $\Delta l/l = 0.5$ , and input shear  $\Delta w/l = 0.45$ ; (4): ribbon radius  $R = l/\pi = 108$  mm, width  $w = 8$  mm, thickness  $b = 0.2$  mm, Poisson's ratio  $\nu = 0.3$ , Young's modulus  $E = 1$  GPa, density  $\rho = 1000$  kg/m<sup>3</sup>, and input twist  $\phi = \pi/2$ . For the first two cases, the ribbon end deflection,  $z_{\text{end}}$ , is used to quantify the deformed configuration; while the midpoint height,  $z_{\text{mid}}$ , is used for the last two scenarios. In Fig. E.20(A)–(D), we plot the relative error as a function of nodal number for four cases. Here, the relative error is defined as  $\text{Error} = \frac{|z_{\text{end}} - z_{\text{end,true}}|}{|z_{\text{end,true}}|}$  (or  $\text{Error} = \frac{|z_{\text{mid}} - z_{\text{mid,true}}|}{|z_{\text{mid,true}}|}$ ), where the true data is obtained when  $N = 200$ . The error would decrease as the enlargement of nodal number, and the relative error would always be less than 1% when  $N = 100$ .

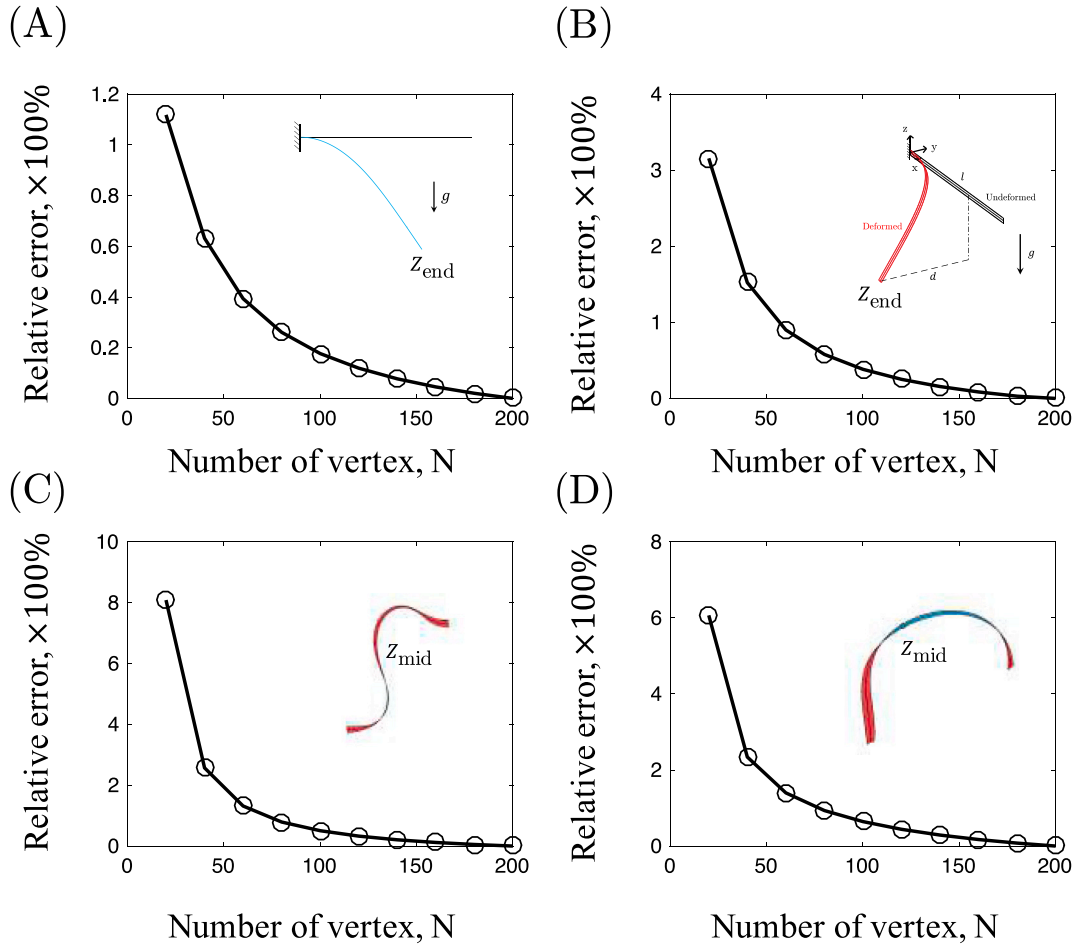


Fig. E.20. Convergent study for (A) Cantilever beam; (B) Lateral-torsional buckling of beams; (C) Shear induced bifurcation of pre-buckled ribbons; and (D) Twist-induced snapping in bent ribbons.

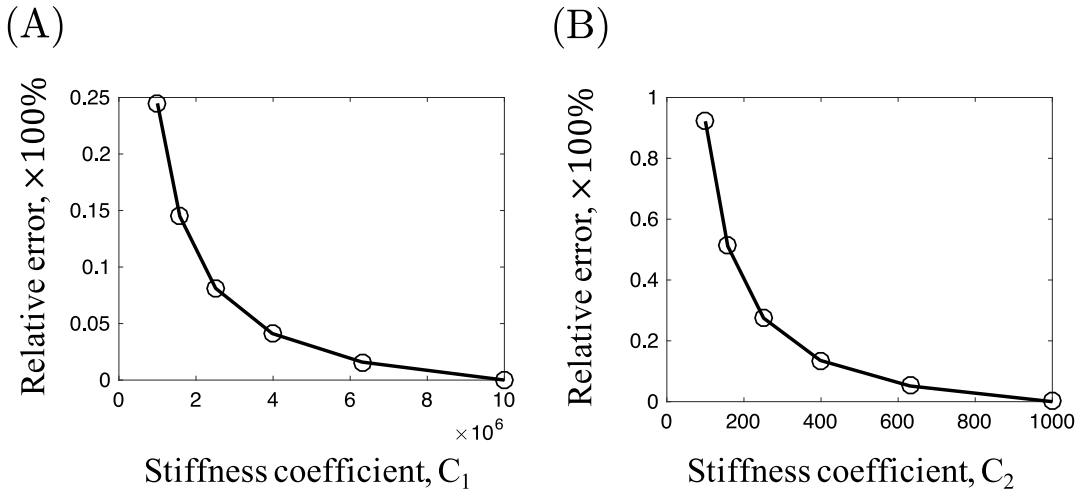


Fig. F.21. Convergent study for (A)  $C_1$  parameter and (B)  $C_2$  parameter.

## Appendix F. Numerical treatment of penalty-based multiplier

In this appendix, we discuss the numerical issue when  $EA \gg EI_2$  (or  $EI_1 \gg EI_2$ ). It is known that the numerical issue would appear when  $EA \gg EI_2$ , which is the case for a ribbon with extremely large length to thickness ratio. However,  $EA$  is only a penalty parameter and has no contribution to the final result as long as it is large enough.

We here demonstrate that the penalty parameter may not need to be physically correct, and use lateral-torsional buckling of beams as an example. Here, all physical parameters are identical to the previous convergent study scenario. The effective parameter is  $EI_2$  and  $GJ$ , while  $EA$  and  $EI_1$  are meaningless as long as they are large enough. We use  $EA = C_1 EI_2$  and  $EI_1 = C_2 EI_2$ . In Fig. F.21(A), we plot the relative error as a function of  $C_1$ , with  $C_2$  fixed as  $10^3$ ; and in Fig. F.21(B),

we plot the relative error as a function of  $C_2$ , with  $C_1$  fixed as  $10^7$ . The error is compared with the result when  $C_1 = 10^7$  and  $C_2 = 10^3$ , which are large enough. The final result almost keep constant (with error less than 1%) as the increase of stiffness. Numerical issue would appear if we continue increasing  $C_1$  and  $C_2$ , and in this case a smaller time step is required. In conclusion, if the real physical stiffness ( $EA$  or  $EI_1$ ) is too large and brings numerical issue, the artificial stiffness can be used as long as it could show good convergence. In our numerical experiments, this type of numerical treatment is used (with verification on convergence) once  $EA \gg EI_2$  (or  $EI_1 \gg EI_2$ ) and numerical issue appears.

## References

- Ameline, O., Haliyo, S., Huang, X., Cognet, J.A., 2017. Classifications of ideal 3D elastica shapes at equilibrium. *J. Math. Phys.* 58 (6), 062902.
- Antman, S.S., Jordan, K.B., 1975. 5.—Qualitative aspects of the spatial deformation of non-linearly elastic rods. *Proc. R. Soc. Edinburgh Sec. A: Math.* 73, 85–105.
- Antman, S.S., Kenney, C.S., 1981. Large buckled states of nonlinearly elastic rods under torsion, thrust, and gravity. *Arch. Ration. Mech. Anal.* 76 (4), 289–338.
- Audoly, B., Clauvelin, N., Brun, P.-T., Bergou, M., Grinspun, E., Wardetzky, M., 2013. A discrete geometric approach for simulating the dynamics of thin viscous threads. *J. Comput. Phys.* 253, 18–49.
- Audoly, B., Lestringant, C., 2021. Asymptotic derivation of high-order rod models from non-linear 3D elasticity. *J. Mech. Phys. Solids* 148, 104264.
- Audoly, B., Neukirch, S., 2021. A one-dimensional model for elastic ribbons: a little stretching makes a big difference. *J. Mech. Phys. Solids* 104457.
- Audoly, B., Pomeau, Y., 2010. *Elasticity and Geometry: From Hair Curls To the Non-Linear Response of Shells*. Oxford University Press.
- Auricchio, F., da Veiga, L.B., Kiendl, J., Lovadina, C., Reali, A., 2016. Isogeometric collocation mixed methods for rods. *Discrete Contin. Dyn. Syst.-S* 9 (1), 33.
- Baek, C., Reis, P.M., 2019. Rigidity of hemispherical elastic gridshells under point load indentation. *J. Mech. Phys. Solids* 124, 411–426.
- Baek, C., Sageman-Furnas, A.O., Jawed, M.K., Reis, P.M., 2018. Form finding in elastic gridshells. *Proc. Natl. Acad. Sci.* 115 (1), 75–80.
- Baraff, D., Witkin, A., 1998. Large steps in cloth simulation. In: *Proceedings of the 25th Annual Conference on Computer Graphics and Interactive Techniques*. ACM, pp. 43–54.
- Bauer, T., Banzer, P., Karimi, E., Orlov, S., Rubano, A., Marrucci, L., Santamato, E., Boyd, R.W., Leuchs, G., 2015. Observation of optical polarization Möbius strips. *Science* 347 (6225), 964–966.
- Béda, P., Steindl, A., Troger, H., 1992. Postbuckling of a twisted prismatic rod under terminal thrust. *Dyn. Stab. Syst.* 7 (4), 219–232.
- Bergou, M., Audoly, B., Vouga, E., Wardetzky, M., Grinspun, E., 2010. Discrete viscous threads. *ACM Trans. Graph.* 29 (4), 116.
- Bergou, M., Wardetzky, M., Robinson, S., Audoly, B., Grinspun, E., 2008. Discrete elastic rods. *ACM Trans. Graph.* 27 (3), 63.
- Bonet, J., Wood, R.D., 1997. *Nonlinear Continuum Mechanics for Finite Element Analysis*. Cambridge University Press.
- Bridson, R., Marino, S., Fedkiw, R., 2005. Simulation of clothing with folds and wrinkles. In: *ACM SIGGRAPH 2005 Courses*. ACM, p. 3.
- Brunetti, M., Favata, A., Vidoli, S., 2020. Enhanced models for the nonlinear bending of planar rods: localization phenomena and multistability. *Proc. R. Soc. Lond. Ser. A Math. Phys. Eng. Sci.* 476 (2242), 20200455.
- Buzano, E., 1986. Secondary bifurcations of a thin rod under axial compression. *SIAM J. Math. Anal.* 17 (2), 312–321.
- Caetano, E.W., Freire, V.N., Dos Santos, S., Galvao, D.S., Sato, F., 2008. Möbius and twisted graphene nanoribbons: Stability, geometry, and electronic properties. *J. Chem. Phys.* 128 (16), 164719.
- Charrondière, R., Bertails-Descoubes, F., Neukirch, S., Romero, V., 2020. Numerical modeling of inextensible elastic ribbons with curvature-based elements. *Comput. Methods Appl. Mech. Engrg.* 364, 112922.
- Coleman, B.D., Swigon, D., 2004. Theory of self-contact in kirchhoff rods with applications to supercoiling of knotted and unknotted DNA plasmids. *Phil. Trans. R. Soc. A* 362 (1820), 1281–1299.
- De Borst, R., Crisfield, M.A., Remmers, J.J., Verhoosel, C.V., 2012. *Nonlinear Finite Element Analysis of Solids and Structures*. John Wiley & Sons.
- Dias, M.A., Audoly, B., 2014. A non-linear rod model for folded elastic strips. *J. Mech. Phys. Solids* 62, 57–80.
- Dias, M.A., Audoly, B., 2015. Wunderlich, meet kirchhoff: A general and unified description of elastic ribbons and thin rods. *J. Elasticity* 119 (1–2), 49–66.
- Dias, M.A., Dudte, L.H., Mahadevan, L., Santangelo, C.D., 2012. Geometric mechanics of curved crease origami. *Phys. Rev. Lett.* 109 (11), 114301.
- Dias, M.A., Santangelo, C.D., 2012. The shape and mechanics of curved-fold origami structures. *Europhys. Lett.* 100 (5), 54005.
- Doedel, E.J., 2007. Lecture notes on numerical analysis of nonlinear equations. In: *Numerical Continuation Methods for Dynamical Systems*. Springer, pp. 1–49.
- Goriely, A., Nizette, M., Tabor, M., 2001. On the dynamics of elastic strips. *J. Nonlinear Sci.* 11 (1), 3–45.
- Goyal, S., Perkins, N.C., Lee, C.L., 2005. Nonlinear dynamics and loop formation in Kirchhoff rods with implications to the mechanics of DNA and cables. *J. Comput. Phys.* 209 (1), 371–389.
- Greco, L., Cuomo, M., 2016. An isogeometric implicit G1 mixed finite element for Kirchhoff space rods. *Comput. Methods Appl. Mech. Engrg.* 298, 325–349.
- Grinspun, E., Hirani, A.N., Desbrun, M., Schröder, P., 2003. Discrete shells. In: *Proceedings of the 2003 ACM SIGGRAPH/Eurographics Symposium on Computer Animation*. Eurographics Association, pp. 62–67.
- Han, D., Pal, S., Liu, Y., Yan, H., 2010. Folding and cutting DNA into reconfigurable topological nanostructures. *Nature Nanotechnol.* 5 (10), 712.
- Han, M., Wang, H., Yang, Y., Liang, C., Bai, W., Yan, Z., Li, H., Xue, Y., Wang, X., Akar, B., et al., 2019. Three-dimensional piezoelectric polymer microsystems for vibrational energy harvesting, robotic interfaces and biomedical implants. *Nat. Electron.* 2 (1), 26.
- Hoffman, K.A., Manning, R.S., Maddocks, J.H., 2003. Link, twist, energy, and the stability of DNA minicircles. *Biopolymers: Orig. Res. Biomol.* 70 (2), 145–157.
- Huang, W., 2021. *Computational Methods in Slender Structures and Soft Robots* (Doctoral Dissertation). UCLA.
- Huang, W., Huang, X., Majidi, C., Jawed, M.K., 2020a. Dynamic simulation of articulated soft robots. *Nature Commun.* 11 (1), 1–9.
- Huang, W., Jawed, M.K., 2019. Newmark-Beta method in discrete elastic rods algorithm to avoid energy dissipation. *J. Appl. Mech.* 86 (8), 084501.
- Huang, W., Ma, C., Qin, L., 2021a. Snap-through behaviors of a pre-deformed ribbon under midpoint loadings. *Int. J. Solids Struct.* 111184.
- Huang, W., Qin, L., Khalid Jawed, M., 2021b. Numerical method for direct solution to form-finding problem in convex gridshell. *J. Appl. Mech.* 88 (2), 021012.
- Huang, W., Wang, Y., Li, X., Jawed, M.K., 2020b. Shear induced supercritical pitchfork bifurcation of pre-buckled bands, from narrow strips to wide plates. *J. Mech. Phys. Solids* 145, 104168.
- Hughes, T.J., 2012. *The Finite Element Method: Linear Static and Dynamic Finite Element Analysis*. Courier Corporation.
- Jawed, M.K., Da, F., Joo, J., Grinspun, E., Reis, P.M., 2014. Coiling of elastic rods on rigid substrates. *Proc. Natl. Acad. Sci.* 111 (41), 14663–14668.
- Jawed, M.K., Novelia, A., O'Reilly, O.M., 2018. *A Primer on the Kinematics of Discrete Elastic Rods*. Springer.
- Kehrbach, S., Maddocks, J., 1999. Elastic rods, rigid bodies, quaternions and the last quadrature. In: *Localization and Solitary Waves in Solid Mechanics*. World Scientific, pp. 181–200.
- Kiendl, J., Auricchio, F., da Veiga, L.B., Lovadina, C., Reali, A., 2015. Isogeometric collocation methods for the Reissner–Mindlin plate problem. *Comput. Methods Appl. Mech. Engrg.* 284, 489–507.
- Koens, L., Lauga, E., 2016. Slender-ribbon theory. *Phys. Fluids* 28 (1), 013101.
- Kumar, A., Handral, P., Bhandari, C.D., Karmakar, A., Rangarajan, R., 2020. An investigation of models for elastic ribbons: Simulations & experiments. *J. Mech. Phys. Solids* 143, 104070.
- Kumar, A., Handral, P., Bhandari, D., Rangarajan, R., 2021. More views of a one-sided surface: mechanical models and stereo vision techniques for Möbius strips. *Proc. R. Soc. Lond. Ser. A Math. Phys. Eng. Sci.* 477 (2250), 20210076.
- Lestringant, C., Audoly, B., 2020. Asymptotically exact strain-gradient models for nonlinear slender elastic structures: a systematic derivation method. *J. Mech. Phys. Solids* 136, 103730.
- Li, S., Han, M., Rogers, J.A., Zhang, Y., Huang, Y., Wang, H., 2019. Mechanics of buckled serpentine structures formed via mechanics-guided, deterministic three-dimensional assembly. *J. Mech. Phys. Solids* 125, 736–748.
- Liu, Y., Wang, X., Xu, Y., Xue, Z., Zhang, Y., Ning, X., Cheng, X., Xue, Y., Lu, D., Zhang, Q., et al., 2019. Harnessing the interface mechanics of hard films and soft substrates for 3D assembly by controlled buckling. *Proc. Natl. Acad. Sci.* 116 (31), 15368–15377.
- Luo, K., Hu, H., Liu, C., Tian, Q., 2017. Model order reduction for dynamic simulation of a flexible multibody system via absolute nodal coordinate formulation. *Comput. Methods Appl. Mech. Engrg.* 324, 573–594.
- Manning, R.S., Maddocks, J.H., 1999. Symmetry breaking and the twisted elastic ring. *Comput. Methods Appl. Mech. Engrg.* 170 (3–4), 313–330.
- Moore, A., Healey, T.J., 2015. Computation of unconstrained elastic equilibria of complete Möbius bands and their stability. *arXiv preprint arXiv:1509.00147*.
- Nan, K., Kang, S.D., Li, K., Yu, K.J., Zhu, F., Wang, J., Dunn, A.C., Zhou, C., Xie, Z., Agne, M.T., et al., 2018. Compliant and stretchable thermoelectric coils for energy harvesting in miniature flexible devices. *Sci. Adv.* 4 (11), eaau5849.
- Neukirch, S., Audoly, B., 2021. A convenient formulation of sadowsky model for elastic ribbons.
- Nizette, M., Goriely, A., 1999. Towards a classification of Euler–Kirchhoff filaments. *J. Math. Phys.* 40 (6), 2830–2866.
- Panetta, J., Konaković-Luković, M., Isvoranu, F., Bouleau, E., Pauly, M., 2019. X-Shells: A new class of deployable beam structures. *ACM Trans. Graph.* 38 (4), 83.
- Raux, P., Reis, P.M., Bush, J., Clanet, C., 2010. Rolling ribbons. *Phys. Rev. Lett.* 105 (4), 044301.

- Romero, V., Ly, M., Rasheed, A.-H., Charrondière, R., Lazarus, A., Neukirch, S., Bertails-Descoubes, F., 2021. Physical validation of simulators in computer graphics: A new framework dedicated to slender elastic structures and frictional contact. *ACM Trans. Graph.*
- Sadowsky, M., 1930. Ein Elementarer Beweis Für Die Existenz Eines Abwickelbaren Möbiusschen Bandes Und Zurückführung Des Geometrischen Problems Auf Ein Variationsproblem.
- Sano, T.G., Wada, H., 2019. Twist-induced snapping in a bent elastic rod and ribbon. *Phys. Rev. Lett.* 122 (11), 114301.
- Shabana, A.A., 1996. An Absolute Nodal Coordinate Formulation for the Large Rotation and Deformation Analysis of Flexible Bodies. Technical Report, Department of Mechanical Engineering, University of Illinois At Chicago.
- Shen, Z., Huang, J., Chen, W., Bao, H., 2015. Geometrically exact simulation of inextensible ribbon. *Comput. Graph. Forum* 34 (7), 145–154.
- Shield, R., 1992. Bending of a beam or wide strip. *Quart. J. Mech. Appl. Math.* 45 (4), 567–573.
- Simo, J.C., 1985. A finite strain beam formulation. The three-dimensional dynamic problem. Part I. *Comput. Methods Appl. Mech. Engrg.* 49 (1), 55–70.
- Simo, J.C., Vu-Quoc, L., 1986. A three-dimensional finite-strain rod model. Part II: Computational aspects. *Comput. Methods Appl. Mech. Engrg.* 58 (1), 79–116.
- Starostin, E.L., 1996. Three-dimensional shapes of looped DNA. *Meccanica* 31 (3), 235–271.
- Starostin, E., van der Heijden, G., 2008. Tension-induced multistability in inextensible helical ribbons. *Phys. Rev. Lett.* 101 (8), 084301.
- Starostin, E., van der Heijden, G., 2015. Equilibrium shapes with stress localisation for inextensible elastic Möbius and other strips. *J. Elasticity* 119 (1–2), 67–112.
- Starostin, E., Van Der Heijden, G., 2007. The shape of a Möbius strip. *Nature Mater.* 6 (8), 563.
- Sun, J., Tian, Q., Hu, H., Pedersen, N.L., 2019. Axially variable-length solid element of absolute nodal coordinate formulation. *Acta Mech. Sinica* 35 (3), 653–663.
- Tanaka, F., Takahashi, H., 1985. Elastic theory of supercoiled DNA. *J. Chem. Phys.* 83 (11), 6017–6026.
- Tang, Y., Hu, H., Tian, Q., 2021. A condensed algorithm for adaptive component mode synthesis of viscoelastic flexible multibody dynamics. *Internat. J. Numer. Methods Engrg.* 122 (2), 609–637.
- Tobias, I., Coleman, B.D., Olson, W.K., 1994. The dependence of DNA tertiary structure on end conditions: theory and implications for topological transitions. *J. Chem. Phys.* 101 (12), 10990–10996.
- Van der Heijden, G., Neukirch, S., Goss, V., Thompson, J., 2003. Instability and self-contact phenomena in the writhing of clamped rods. *Int. J. Mech. Sci.* 45 (1), 161–196.
- Van der Heijden, G., Thompson, J., 1998. Lock-on to tape-like behaviour in the torsional buckling of anisotropic rods. *Physica D* 112 (1–2), 201–224.
- Van der Heijden, G., Thompson, J., 2000. Helical and localised buckling in twisted rods: a unified analysis of the symmetric case. *Nonlinear Dynam.* 21 (1), 71–99.
- Wadati, M., Tsuru, H., 1986. Elastic model of looped DNA. *Physica D* 21 (2–3), 213–226.
- Wang, X., Zheng, X., Ni, M., Zou, L., Zeng, Z., 2010. Theoretical investigation of Möbius strips formed from graphene. *Appl. Phys. Lett.* 97 (12), 123103.
- Wood, R.D., Zienkiewicz, O., 1977. Geometrically nonlinear finite element analysis of beams, frames, arches and axisymmetric shells. *Comput. Struct.* 7 (6), 725–735.
- Wu, Z.L., Moshe, M., Greener, J., Therien-Aubin, H., Nie, Z., Sharon, E., Kumacheva, E., 2013. Three-dimensional shape transformations of hydrogel sheets induced by small-scale modulation of internal stresses. *Nature Commun.* 4, 1586.
- Wunderlich, W., 1962. Über ein abwickelbares Möbiusband. *Monatshefte Math.* 66 (3), 276–289.
- Xu, Z., Fan, Z., Fu, H., Liu, Y., Zi, Y., Huang, Y., Zhang, Y., 2019. Optimization-based approach for the inverse design of ribbon-shaped three-dimensional structures assembled through compressive buckling. *Phys. Rev. A* 11 (5), 054053.
- Yu, T., Hanna, J., 2019. Bifurcations of buckled, clamped anisotropic rods and thin bands under lateral end translations. *J. Mech. Phys. Solids* 122, 657–685.
- Zhang, L., Abbott, J.J., Dong, L., Kratochvil, B.E., Bell, D., Nelson, B.J., 2009. Artificial bacterial flagella: Fabrication and magnetic control. *Appl. Phys. Lett.* 94 (6), 064107.
- Zhao, H., Li, K., Han, M., Zhu, F., Vázquez-Guardado, A., Guo, P., Xie, Z., Park, Y., Chen, L., Wang, X., et al., 2019. Buckling and twisting of advanced materials into morphable 3D mesostructures. *Proc. Natl. Acad. Sci.* 201901193.
- Zienkiewicz, O.C., Taylor, R.L., 2005. *The Finite Element Method for Solid and Structural Mechanics*. Elsevier.